JGR Space Physics

RESEARCH ARTICLE
10.1029/2022JA030866

Key Points:

- Wintertime thermospheric gravity waves (GWs) simulated by a whole atmosphere model are strongly reduced during the January 2017 sudden stratospheric warming (SSW) and the subsequent weak-vortex period
- Observed quiet-time total electron content (TEC) perturbations show reduced amplitudes during the SSW and weak-vortex period as well
- Propagation directions, wavelengths, and periods of the simulated thermospheric GWs agree with observed quiet-time TEC perturbations

Correspondence to:
E. Becker,
erich.becker@nwra.com

Citation:
Becker, E., Goncharenko, L., Harvey, V. L., & Vadas, S. L. (2022). Multi-step vertical coupling during the January 2017 sudden stratospheric warming. *Journal of Geophysical Research: Space Physics*, *127*, e2022JA030866. https://doi.org/10.1029/2022JA030866

Received 20 JUL 2022
Accepted 8 NOV 2022

Multi-Step Vertical Coupling During the January 2017 Sudden Stratospheric Warming

Erich Becker[1], Larisa Goncharenko[2], V. Lynn Harvey[3], and Sharon L. Vadas[1]

[1]NorthWest Research Associates, Boulder, CO, USA, [2]MIT Haystack Observatory, Westford, MA, USA, [3]Laboratory for Atmospheric and Space Physics, University of Colorado Boulder, Boulder, CO, USA

Abstract This study analyzes a simulation of the Arctic winter 2016–2017 with focus on multi-step vertical coupling (MSVC) by primary, secondary, and higher-order gravity waves (GWs). We employ the HIgh Altitude Mechanistic general Circulation Model with nudging of the large scales to MERRA-2 reanalysis. Simulation results confirm the well-known effects from primary GWs in the winter middle atmosphere regarding strong westward GW drag and a warm winter polar stratopause during the strong-vortex period in late December 2016, as well as weak eastward GW drag and mesospheric cooling during the sudden stratospheric warming (SSW) in late January and early February 2017. Since the amplitudes of the primary GWs that dissipate in the middle atmosphere are weaker for a reversed or weakened polar vortex, the theory for secondary GW generation predicts reduced MSVC in this case. This is confirmed by strongly reduced secondary and higher-order GW amplitudes during the SSW and the weak-vortex period in February. The wintertime higher-order GWs show partial concentric ring structures above their sources in the lower thermosphere. We find that mostly those higher-order GWs propagate to higher altitudes that have horizontal propagation directions against the tidal winds. The simulated GWs at 300 km height and observed perturbations of total electron content over Europe and North America during selected days of low geomagnetic activity show very good agreement regarding (a) the wave characteristics and (b) the reduction of amplitudes during the SSW and early February as compared to late December.

Plain Language Summary We analyze the Arctic winter 2016–2017 using a whole atmosphere model with resolved gravity waves (GWs) and nudging of the large scales to MERRA-2 reanalysis. Model results confirm the well-known effects from primary GWs in the winter middle atmosphere regarding strong westward GW drag and a warm winter polar stratopause during the strong-vortex period in late December 2016, as well as weak eastward GW drag and mesospheric cooling during the sudden stratospheric warming (SSW), which started in late January 2017 and was followed by a weak vortex in February. Since secondary and higher-order GWs are the predominant GWs in the winter mesopause region and thermosphere, the vertical coupling from the lower to the upper atmosphere by GWs is termed multi-step vertical coupling (MSVC). We find that MSVC is strongly reduced during and after the SSW. The simulated GWs at 300 km height and observed total electron content (TEC) perturbations over Europe and North America during days of low geomagnetic activity show very good agreement regarding the wave characteristics. Furthermore, we find a clear reduction in the TEC perturbation amplitudes during and after the SSW. This agreement between model and observations strongly suggests that quiet-time TEC perturbations in the winter thermosphere are caused by GWs from MSVC.

1. Introduction

Major sudden stratospheric warming (SSW) events occur typically in three out of four winter seasons in the Northern Hemisphere (NH) (Butler et al., 2017). They are characterized by a temporary increase of stratospheric temperatures by up to 50 K or more at high latitudes. This phenomenon was first observed about 70 years ago over Berlin (Scherhag, 1952) and remained unexplained for about 20 years. Matsuno (1971) invoked quasi-linear dynamics of quasi-geostrophic flow and assumed a stationary planetary Rossby wave with zonal wavenumber 2 forced at the tropopause. With these idealizations, Matsuno successfully simulated an SSW for the first time in a three-dimensional numerical model (see also Andrews et al., 1987, Ch. 6). The applicability of Matsuno's model to the real atmosphere was, however, limited because (a) a superposition of several zonal wavenumbers was neglected, but is now known to be important, particularly during the preconditioning of the polar vortex (e.g., McIntyre, 1982), (b) the anomalous residual circulation associated with the SSW was not superposed on

the climatological mean residual circulation, resulting in a zonal-mean momentum budget that did not capture important features of realistic events (e.g., Dunkerton et al., 1981), and (c) Matsuno's model could not simulate the restoration of the polar vortex after the event since his model had no radiative forcing. It is furthermore worth noting that quasi-geostrophic theory is generally limited since non-balanced ageostrophic motions (including gravity waves [GWs]) and nonlinear advection by the residual circulation are neglected, but play a significant role also during an SSW event. Beside these limitations, the necessary tropospheric forcing and resulting stratospheric dynamics of an SSW can well be understood on the basis of Matsuno's model.

The dynamics of the mesosphere during an SSW is usually characterized by significant cooling, as was first reported by Labitzke (1972). Holton (1983) explained this mesospheric cooling by taking the momentum deposition from upward propagating GWs into account. More specifically, he used a simplified general circulation model (GCM) and showed that the climatological westward GW drag in the winter mesosphere is strongly reduced or even reversed during an SSW, leading to an anomalous equatorward residual flow in the mesosphere at middle latitudes that is balanced by an anomalous residual upwelling over the polar cap, thereby causing the mesospheric cooling. Details of this process were extensively studied since then using more comprehensive models (e.g., Dunkerton & Butchart, 1984; Siskind et al., 2005; 2010; Tomikawa et al., 2021; Zülicke et al., 2018).

The variability of momentum deposition by GWs is also crucial when a major SSW is followed by a strong recovery of the polar vortex, which is often accompanied by an elevated winter polar stratopause (ES). The phenomenon of an ES was first reported by Manney et al. (2008, 2009) and Randall et al. (2009), and was later simulated using GCMs with parameterized GWs (e.g., Chandran et al., 2013; Funke et al., 2017; Limpasuvan et al., 2012; McLandress et al., 2013; Siskind et al., 2010) and resolved GWs (Tomikawa et al., 2021; Zülicke & Becker, 2013). It can be understood by noting that a strong vortex allows westward propagating GWs of tropospheric origin to propagate into the upper mesosphere before they become dynamically unstable and dissipate. The resulting westward GW drag shortly after the SSW is then located at altitudes higher than usual. As a result, the new winter polar stratopause shortly after the SSW is elevated as well. During this phase, the elevated westward GW drag is not fully balanced by the residual circulation such that the mesospheric part of the polar vortex weakens. This causes the westward propagating GWs to dissipate at somewhat lower altitudes, causing the stratopause to shift to lower altitudes as well. This downward progression ceases when a quasi equilibrium between the wave driving and the residual circulation is reached, which is typically the case when the winter polar stratopause is again at its climatological altitude. A summary of our current understanding of SSW events, including effects in the troposphere and the mesosphere, can be found in the recent review paper by Baldwin et al. (2021).

A model study of a major SSW by Liu and Roble (2002) using the TIME GCM with parameterized GWs showed that the mesospheric cooling can reach as high as the winter mesopause region. This vertical extent of the mesospheric cooling was later confirmed by Cho et al. (2004) based on temperature measurements using airglow. Liu and Roble (2002) also found an anomalous warming of the lower thermosphere and anomalous eastward zonal winds in the mesopause region during the SSW. An explanation of the simulated thermospheric warming was that the anomalous eastward winds around the winter mesopause provided favorable propagation conditions for westward propagating GWs. Such GWs could propagate to these altitudes in the TIME GCM because they were not entirely filtered by the stratospheric wind reversal, which in turn was presumably because the launch level for the parameterized GWs in the TIME GCM was in the mid stratosphere at 10 hPa (about 30 km height). The dissipation of the westward GWs in the lower thermosphere during the SSW then resulted in enhanced downwelling and increased temperatures over the winter pole. Given the specific setup of the GW parameterization in the TIME GCM as used by Liu and Roble (2002), it is not clear whether the winter polar lower thermosphere exhibits anomalously high temperatures during a major SSW event or not.

Also observational studies do not give a clear picture of the large-scale thermal effects in the thermosphere during SSW events. For example, alternating regions of warming in the lower thermosphere and cooling above ∼150 km at a middle latitude location (42.6°N) were reported by Goncharenko and Zhang (2008). A moderate 20−50 K warming was reported in EISCAT lower thermospheric ion temperatures (Kurihara et al., 2010), and lower thermospheric warming was also seen in satellite data from the Michelson Interferometer for Passive Atmospheric Sounding (Funke et al., 2010). In the upper thermosphere, an SSW-associated cooling of ∼100−150 K at high latitudes was identified in ground-based observations (Conde & Nicolls, 2010), while slight temperature reductions were seen in heavily averaged satellite observations reported by Yamazaki et al. (2015). Other upper atmospheric effects during SSW events have been studied by, for example, Fuller-Rowell et al. (2010, 2011) and

Goncharenko et al. (2010) who focused on thermal tides and zonal-mean fields in the thermosphere and on the ionosphere at low latitudes, respectively. A recent overview about upper atmospheric effects during SSW events can be found in Goncharenko et al. (2021).

Specific information about the response of GWs in the thermosphere during SSW events can be deduced from observations of Traveling Ionospheric Disturbances (TIDs). For example, Frissell et al. (2016) and Nayak and Yiğit (2019) found that the wintertime TID activity in the NH is correlated to the strength of the polar vortex, thereby suggesting a weakening of thermospheric GW activity during SSW events. Owing to recent modeling studies (Becker & Vadas, 2020; Vadas & Becker, 2019) and analysis of satellite observations in the thermosphere (Vadas et al., 2019), it is very likely that GWs in the winter thermosphere are often not primary GWs of tropospheric origin, but are rather secondary and higher-order GWs that result from multi-step vertical coupling (hereafter: MSVC). MSVC can be understood based on the theory described in Vadas et al. (2003, 2018), but may be more complicated for more realistic flows (Fritts et al., 2020). In simple terms (see also Vadas & Becker, 2019, their Figure 21), MSVC means that the spatially localized and intermittent momentum deposition by a GW packet (hereafter: body force) leads to an imbalance of the ambient flow. This imbalance results in the generation of new GWs that propagate into various directions, except perpendicular to the direction of the body force. For example, when secondary GWs are generated in the winter mesosphere from the momentum deposition of westward propagating primary GWs, these secondary GWs will have predominant westward and eastward intrinsic propagation directions. The eastward propagating secondary waves have favorable conditions to propagate into the mesopause region because of the westward vertical zonal wind shear associated with the polar vortex in the mesosphere. When these secondary GWs break in the winter mesopause region, they exert an eastward drag. According to Becker and Vadas (2018), this effect can explain the observed predominant eastward wind direction in the wintertime mesopause region at middle to high latitudes during medium-to-strong polar vortex periods, as is found in observations (de Wit et al., 2017; Hindley et al., 2022; Hoffmann et al., 2010; Smith, 2012; Stober, Janches, et al., 2021). In turn, the dissipation of secondary GWs leads to the generation of tertiary GWs that can propagate well into the thermosphere (Vadas & Becker, 2019). These wintertime thermospheric GWs generally have much larger horizontal phase speeds and vertical wavelengths than what is typically observed in the lower and middle atmosphere. The model study by Becker and Vadas (2020) showed that wintertime higher-order GWs caused by MSVC can explain the observed southward propagation of TIDs during local noon and afternoon (e.g., Crowley & Rodrigues, 2012), as well as the observed thermospheric GW hot spot over the Southern Andes/Antarctic Peninsula during southern hemispheric winter (Park et al., 2014; Trinh et al., 2018; Xu et al., 2021).

The effects from secondary and higher-order GWs are excluded in conventional whole atmosphere models with parameterized GWs. Also the new generation of transient GW schemes that are currently being developed rely on the specification of launch level parameters at a certain altitude and exclude higher-order GWs (e.g., Bölöni et al., 2021). According to current wisdom, the simulation of MSVC requires the explicit simulation of GWs. The HIgh Altitude Multi-scale general Circulation Model (HIAMCM) explicitly resolves GWs from the surface up to about 450 km height. MSVC in the winter hemisphere is simulated by the HIAMCM because GW-mean flow interactions resulting in new GWs are consistently induced by a macro-turbulent vertical and horizontal diffusion scheme (Becker, 2009; Becker & Vadas, 2020). This scheme includes molecular viscosity for both vertical and horizontal diffusion. More recently, Becker et al. (2022) developed nudging to MERRA-2 reanalysis for the HIAMCM. This nudging is performed in spectral space and restricted to the large scales. In the present study we employ the nudged HIAMCM to simulate MSVC and the resulting GWs in the winter thermosphere during an SSW event. We chose the NH winter 2016–2017 with an SSW from about 25 January to 6 February 2017 because there was generally low geomagnetic activity during this winter, thereby allowing us to associate observed perturbations in total electron content (TEC) with thermospheric GWs "from below." The only exception is for the period from 31 January to 7 February 2017, when increase in geomagnetic activity could lead to ionospheric perturbations of auroral origin in addition to the GWs from below.

In Sections 2 and 3, we briefly describe the HIAMCM, as well as our analysis of observed TEC perturbations over Europe and over North America. Section 4 presents zonal-mean results from the HIAMCM simulation for the winter 2016–2017. In Sections 5 and 6, we present and discuss our main results regarding the simulated GWs in the thermosphere and the related TEC perturbations. Our summary and concluding remarks are presented in Section 7.

2. Model Description

The HIAMCM is based on standard spectral dynamical core with a terrain-following hybrid vertical coordinate (Simmons & Burridge, 1981). It is currently run at a spectral resolution of T256 (triangular spectral truncation at a total horizontal wavenumber of 256), which corresponds to a horizontal grid-spacing of ∼52 km and a shortest resolved horizontal wavelength of $\lambda_h \sim 156$ km. Becker et al. (2022) showed that the effective horizontal resolution of the HIAMCM corresponds to $\lambda_h \sim 200$ km. The vertical level spacing is ∼600−650 m between the boundary layer and 3×10^{-5} hPa ($z \sim 130$ km), and increases with altitude above that level, reaching ∼10 km above ∼300 km. Using 280 full layers, the model top is at 4×10^{-9} hPa, corresponding to $z \sim 450$ km for temperatures of $T \sim 950$ K above ∼250 km. These temperatures correspond to moderate solar maximum conditions, which is applied in the present study.

The dynamical core of the HIAMCM is equipped with a correction for non-hydrostatic dynamics (Becker & Vadas, 2020, Appendix B), which is important in the thermosphere where many of the resolved GWs have high intrinsic frequencies. Furthermore, the dynamical core includes a thermodynamically consistent extension of the equation of state and the sensible heat equation into the thermosphere. This is achieved by specifying the gas constant as a function of the pressure and the heat capacity at constant pressure as a function of the temperature (Becker & Vadas, 2020, their Appendix D).

The HIAMCM includes explicit computations of radiative transfer and water vapor transport, parameterizations of large-scale condensation and moist convection, as well as the full surface energy budget, including full topography and a slab ocean. Macro-turbulent vertical and horizontal diffusion is represented by the Smagorinsky scheme, with both diffusion coefficients depending on the Richardson number, R_i, giving rise to strong wave damping in the troposphere for $R_i \leq 0$, and in the mid stratosphere and farther above for $R_i \leq 0.25$ (Becker, 2009). This three-dimensional diffusion scheme accommodates molecular viscosity. Indeed, molecular viscosity becomes the predominant vertical diffusion coefficient above $z \sim 150$ km in models. In the HIAMCM, molecular viscosity furthermore becomes the predominant horizonal diffusion coefficient above $z \sim 200$ km. As a result, molecular viscosity turns out to be the major dissipation mechanism for GWs in the upper thermosphere (Pitteway & Hines, 1963; Vadas, 2007). Note that in the HIAMCM, this effect of molecular viscosity is strongly due to the horizontal diffusion of momentum and sensible heat. To the best of our knowledge, the HIAMCM is the first GCM that consistently includes molecular viscosity and heat conduction in the horizontal diffusion scheme (Becker & Vadas, 2020, their Section 2 and Appendix A).

To simulate the neutral-ion coupling that leads to damping of the large-scale winds in the thermosphere, the simple ion drag scheme based on the parameters given in Hong and Lindzen (1976) has been extended by adding a diurnal cycle of the ion density (Becker & Vadas, 2020, their Appendix E). This parameterized ion drag is the major dissipation mechanism in the thermosphere for the in situ generated diurnal tide. For the purpose of the present study, another ion drag parameterization has been added that drives the auroral circulation in the polar regions (e.g., Forbes, 2007). This new parameterization is described in Appendix A of this paper.

Nudging to MERRA-2 reanalysis in the troposphere and stratosphere was recently developed for the HIAMCM by Becker et al. (2022). This nudging is performed in spectral space and is restricted to the planetary-scale and synoptic-scale flow. As a result, the explicit simulation of GWs is preserved since GWs are not directly affected by the nudging.

The HIAMCM employs radiation and moist convection schemes that are simplified compared to comprehensive methods used in community models. Furthermore, the model does not include a chemistry module, and ion drag is the only ionospheric process that is accounted for. To distinguish these idealizations from methods employed in comprehensive community models, the HIAMCM is called a "mechanistic model."

We take advantage of the spectral formulation when analyzing model data with respect to resolved GWs and the large-scale flow. Throughout this study, we associate dynamical fields that are spectrally truncated at a total wavenumber of $n = 30$ as the large-scale flow. This corresponds to horizontal scales having $\lambda_h \geq 1{,}350$ km. Accordingly, GW perturbations are defined by the difference between spectral truncation at $n = 256$ (the resolution wavenumber of the model) and $n = 30$, that is, by having 156 km $\leq \lambda_h < 1{,}350$ km.

3. Analysis of TEC Perturbations

Direct observations of Traveling Atmospheric Disturbances (TADs) are relatively rare, although satellite observations in the upper thermosphere revealed average seasonal and solar cycle characteristics of thermospheric GWs (Bruinsma & Forbes, 2008; Garcia et al., 2016; Park et al., 2014). As ionospheric observations are much more common, the bulk of observational information comes from observations of TIDs. Statistical studies conclude that TID characteristics are consistent with properties of GWs (England et al., 2021; Negrea et al., 2016); therefore, TIDs are frequently used as a proxy for TADs.

In this study, we use observations of TIDs determined from GNSS TEC data that are provided by the CEDAR Madrigal database. More specifically, we utilize differential TEC (dTEC), which is based on 100–200 million individual line-of-sight TEC measurements per day. Differential TEC values were computed by removing the background TEC using a Savitsky-Golay filter with a 30-min running window. This analysis was applied to all data segments of line-of-sight measurements between individual GNSS satellites and individual ground-based GNSS receivers. The resulting dTEC data product has been used successfully to study both large-scale and medium-scale TIDs related to geospace phenomena like geomagnetic storms and solar eclipses, and to tropospheric convection (Coster et al., 2017; Jonah et al., 2018; Zhang et al., 2017, 2019). Our analysis excludes the period from 31 January to 7 February 2017, when TEC perturbations could be potentially driven by auroral sources due to the episodic increases in geomagnetic activity to the levels of minor geomagnetic storms (Kp = 3+ to Kp = 5).

4. Zonal-Mean Results for the Northern Winter 2016–2017

The nudged HIAMCM was integrated from 1 December 2016 to 28 February 2017. Figure 1 shows time series from 11 December 2016 to 21 February 2017 of the temperature averaged over the polar cap (from 70 to 90°N) and of the zonal wind averaged over the latitude band from 50 to 70°N. We can infer a period in early winter (e.g., around 27 December) when the polar vortex was quite strong. The vortex then weakened during January and the SSW started in late January. Such a seasonal evolution of the NH polar vortex is quite typical (Harvey et al., 2019). For the particular season investigated here, the stratospheric wind reversal was strongest in the lower mesosphere around 31 January, and the polar vortex started to recover around 6 February. Furthermore, the mean zonal wind did not reverse at the 10 hPa level during the SSW 2017; therefore this SSW was not classified as a major event. Also note that this SSW was not followed by an elevated stratopause because there was only a weak recovery of the polar vortex. The nudged HIAMCM simulates all these features, including the mesospheric cooling during the SSW.

Figure 2 shows the time series of the wave driving in terms of the Eliassen-Palm Flux (EPF) divergence, here averaged from 50 to 70°N. First we computed this quantity from the complete model data. Then we truncated the model data in spectral space at a total wavenumber of $n = 30$ and recalculated the EPF divergence, yielding the wave driving that is mainly due to planetary waves (PWs) which is shown in Figure 2a. This PW EPF divergence includes contributions from quasi-stationary Rossby waves forced in the troposphere, from synoptic-scale Rossby waves in the troposphere, from traveling PWs in the mesosphere and lower thermosphere (MLT), from thermal tides, and even from large-scale inertia GWs. The total EPF divergence with truncation at $n = 256$ minus the PW EPF divergence with truncation at $n = 30$ is the wave driving associated with the resolved GWs (hereafter: GW EPF divergence or GW drag). The latter is shown in the lower panel of Figure 2. As expected, the GW drag in the winter mesosphere is westward before the SSW. This GW drag is strongest when the polar vortex is strongest, which is the case in late December. Such a correlation between the polar vortex and the primary GW drag is well understood and is part of the interhemispheric coupling mechanisms (e.g., Karlsson & Becker, 2016; Karlsson et al., 2009).

The seasonal evolution of the polar vortex in the northern winter hemisphere (strong in December and weaker in January) is caused by the fact that quasi-stationary Rossby waves forced in the troposphere are still weak in early winter because of the inertia of the surface temperature differences between the ocean and land masses, but are increasingly forced as the winter season advances. As a result of the strong polar vortex in early winter, the strong westward GW drag induces a warm winter polar stratopause and a strong westward vertical wind shear in the mesosphere. According to the study of McLandress et al. (2006), this corresponds to a large-scale barotropic/baroclinic instability that leads to the development of eastward traveling PWs in the mesosphere. The eastward

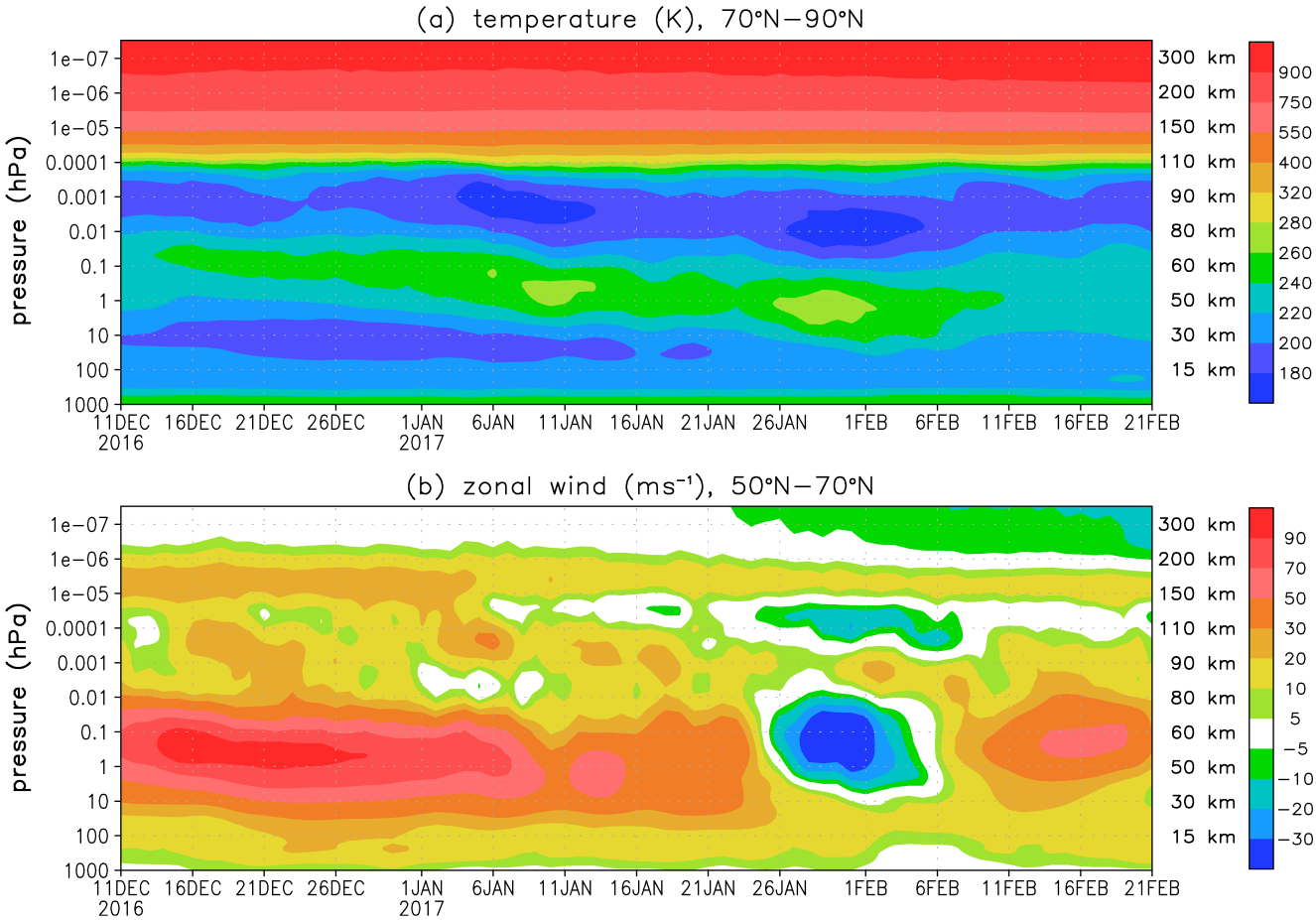

Figure 1. Time series from 11 December 2016 to 21 February 2017 of (a) the simulated temperature averaged over the polar cap (from 70 to 90°N) and (b) the simulated zonal wind averaged over the latitude band from 50 to 70°N. The vertical coordinate is the hybrid-vertical coordinate of the model times 1,013 hPa. Approximate geometric heights are given on the right-hand side of each panel.

PW EPF divergence around 0.1 to 0.01 hPa (60–80 km) prior to about 11 January in Figure 2a likely results from these traveling PWs.

A significant westward PW EPF divergence develops in the stratosphere on 5–11 January and again on 23–31 January. This westward PW EPF divergence is due to quasi-stationary planetary Rossby waves forced in the troposphere. The second burst of this PW EPF divergence culminates in the SSW. The associated changes of the zonal wind (Figure 1b) modifies the predominant propagation direction of the primary GWs. This direction is westward in the lower mesosphere during the winter up until the SSW. During the wind reversal, eastward propagating primary GWs have favorable propagation conditions in the upper stratosphere and mesosphere, such that the primary GW drag becomes eastward. When a weak polar vortex is reestablished in February, the primary GW drag in the mesosphere is again westward.

Figure 2b shows eastward GW drag in the MLT during the whole winter before the SSW. As discussed in earlier studies (Becker & Vadas, 2018, 2020), this eastward GW drag is due mainly to secondary GWs. In our current simulation, the eastward GW drag prior to the SSW extends up to about 1×10^{-5} hPa ($z \sim 140$ km). A weak eastward GW drag in the lower thermosphere is also visible during the SSW and after the SSW. The eastward GW drag at higher altitudes in the thermosphere prior to the SSW and the stripe of eastward PW EPF divergence around 1×10^{-5} hPa throughout the winter will be discussed farther below. Note that the PW EPF divergence in the thermosphere above about 200 km is westward. This is mainly a result of the ion-drag-induced dissipation of tides (Becker, 2017).

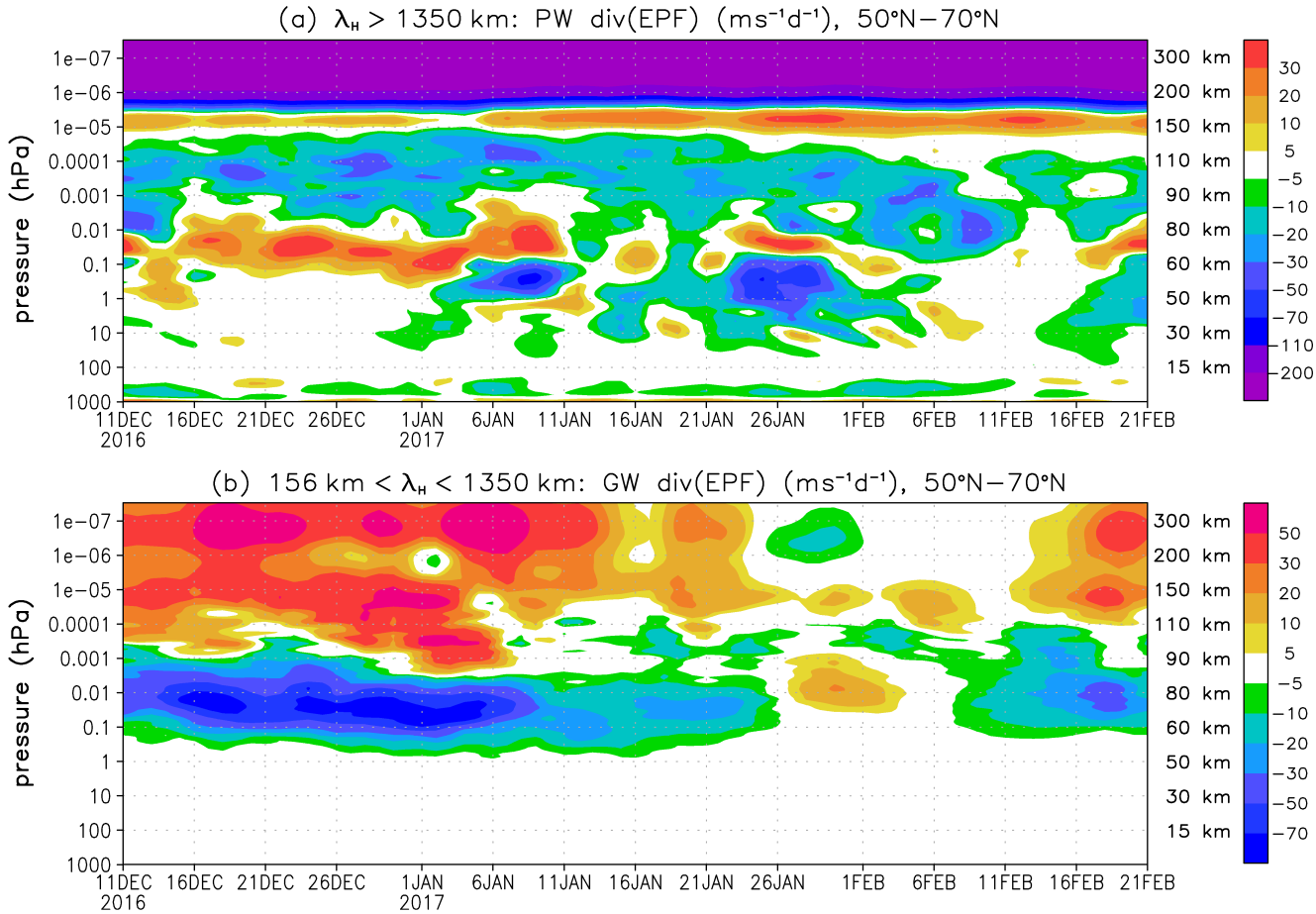

Figure 2. Same as Figure 1, but for the planetary wave Eliassen-Palm Flux (EPF) divergence (panel (a), $\lambda_h \geq 1{,}350$ km) and the gravity wave EPF divergence (panel (b), $\lambda_h < 1{,}350$ km). See also text for definitions.

Figures 3 and 4 show the zonal-mean circulation and the corresponding wave driving of the residual circulation during a period when the polar vortex was strong, averaged from 20 to 31 December 2016 (Figures 3a, 3c, 4a, and 4c), and during the wind reversal associated with the SSW, averaged from 25 January to 5 February 2017 (Figures 3b, 3d, 4b, and 4d). The upper row in Figure 3 shows the zonal-mean temperatures (colors) and the residual mass streamfunctions (contours); the lower row shows the corresponding zonal-mean zonal winds. From Figures 3a and 3b we can infer the warming of the northern polar stratosphere and the corresponding cooling of the mesosphere aloft during the SSW as compared to the situation in late December. Furthermore, the differences of the residual mass streamfunction in the winter middle atmosphere during the two periods confirm that the stratospheric warming and mesospheric cooling over the polar cap are directly caused by an intensification of the residual circulation in the stratosphere and a reversal in the mesosphere, respectively (note the white contours for -10^{-5} and -10^{-3} Mt s^{-1} in the polar winter mesosphere in Figure 3b). These changes of the residual circulation are driven by the changes in the PW and GW EPF divergences, with the former enhancing the stratospheric branch and the latter reversing the mesospheric branch of the residual circulation. This pattern is simulated here with a GW-resolving GCM and is generally consistent with current understanding of the dynamics during an SSW. Note that the steady-state Transformed Eulerian Mean equations apply to a good approximation even during an SSW. Indeed, the transient changes of the zonal-mean zonal wind are due to the residuum of the acceleration (or deceleration) from the Coriolis force plus nonlinear advection by the residual circulation and the deceleration (or acceleration) by the EPF divergence, while the transient temperature changes reflect the residuum of the adiabatic heating (or cooling) plus nonlinear advection by the residual circulation and radiative cooling (or heating) (Andrews et al., 1987; Baldwin et al., 2021; Dunkerton et al., 1981; Holton, 1983; McIntyre, 1982).

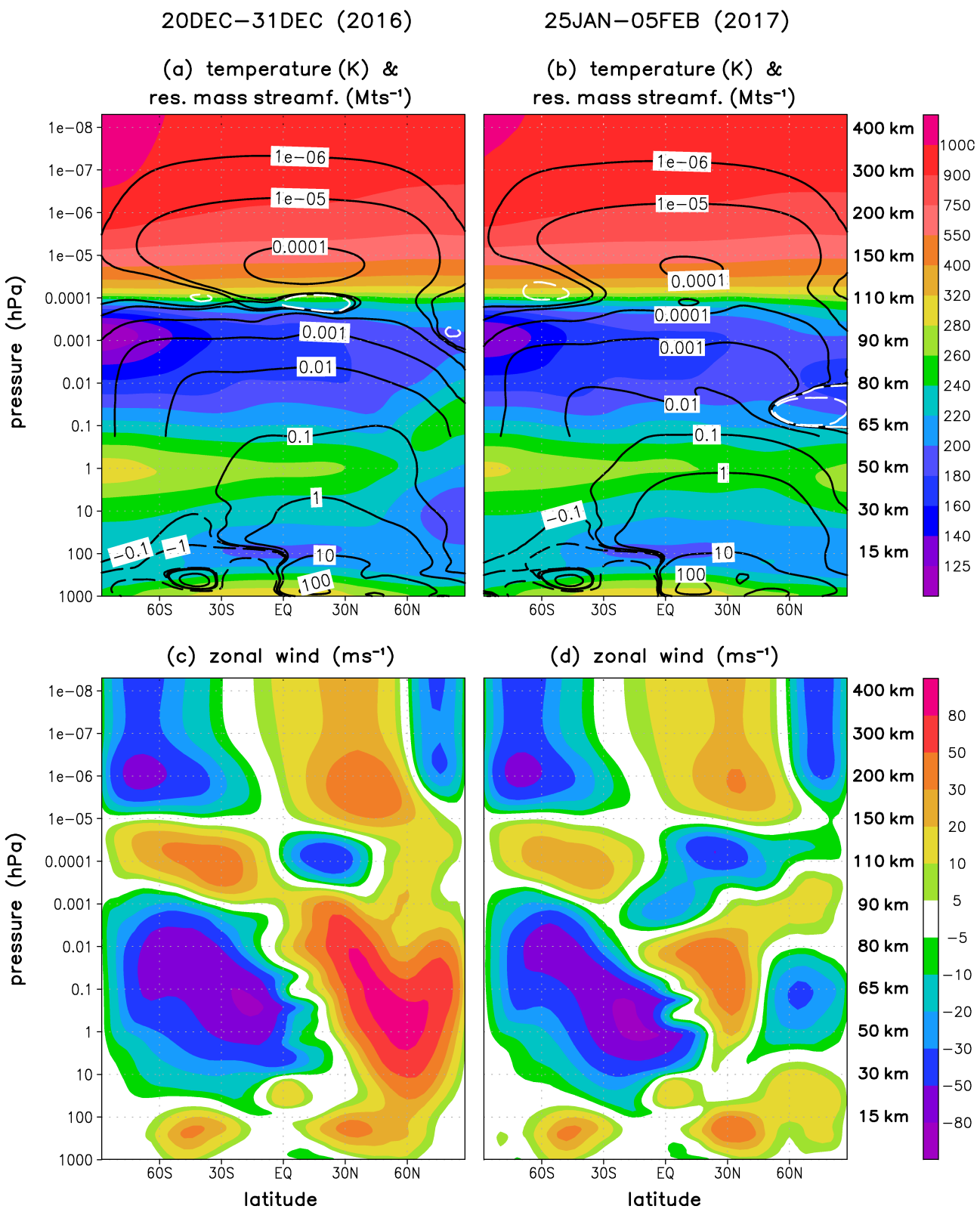

Figure 3. Simulated zonal-mean temperature (upper row, colors) and zonal wind (second row, colors) from 20 to 31 December 2016 (left column) and during 25 January to 5 February 2017 (right column). The black colors in the upper panels show the residual mass streamfunction (plotted for $+10^{-6}$, $\pm10^{-5}$, $+10^{-4}$, $+10^{-3}$, and $+10^{-2}$ Mt s^{-1} above 0.3 hPa, and for ±0.1, ±1, ±10, and $+100$ Mt s^{-1} below 0.1 hPa, 1 Mt = 10^9 kg). Additional white contours show the residual mass streamfunction for -10^{-5} Mt s^{-1} in panel (a), and for -10^{-5} and -10^{-3} Mt s^{-1} in panel (b). The vertical coordinate is the hybrid-vertical coordinate of the model times 1,013 hPa. Approximate geometric heights are given on the right-hand side of panels (b and d).

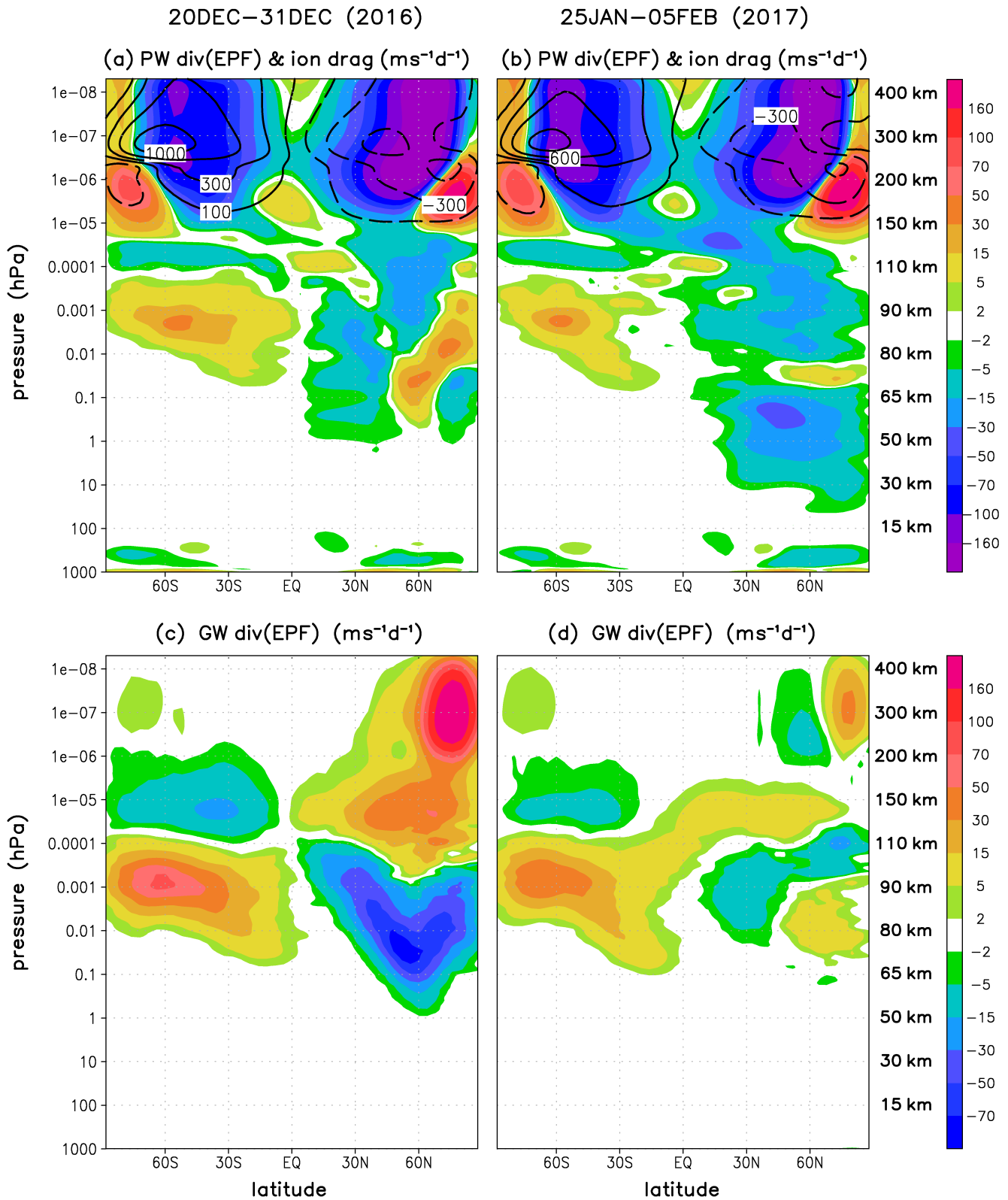

Figure 4. Same as Figure 3, but for the planetary wave Eliassen-Palm Flux (EPF) divergence (colors, upper row) and the gravity wave EPF divergence (colors, lower row). The black contours in the upper panels show the zonal-mean zonal ion drag per unit mass (for ±100, ±300, ±600, and +1,000 m s^{-1} d^{-1}). See text for definitions.

In the present HIAMCM simulation, the mesospheric cooling reaches into the winter polar mesopause region, as was also found by Liu and Roble (2002). In contrast to this former study, our results neither indicate an anomalous zonal-mean eastward wind in the MLT nor a notable warming of the lower thermosphere over the polar cap during the SSW (see Figure 1). The likely reason for these differences is that GW effects in winter mesopause region are due to resolved secondary and higher-order GWs in the HIAMCM, and are due to parameterized primary GWs launched at 10 hPa (about 30 km height) in the TIME GCM used by Liu and Roble (2002). A detailed analysis of the consequences of these different model setups for the simulation of an SSW is beyond the scope of our study.

Figure 3 indicates a warmer summer mesopause during the SSW 2017 than in late December 2016. This is consistent with a weaker eastward GW EPF divergence that drives the equatorward flow in this regime (Figures 4c and 4d). This difference could be the result of the advanced seasonal cycle, of interhemispheric coupling during the SSW (e.g., Becker, 2012; Karlsson et al., 2009), or a combination of both mechanisms. Note that both the PW and GW EPF divergences in Figure 4 are eastward beneath the summer mesosphere. While this is expected for the GW scales, there is an apparent discrepancy to the expected westward EPF divergence from traveling PWs in this region. The reason for the eastward PW EPF divergence beneath the summer mesopause in Figures 4a and 4b is that large-scale inertia GWs give a significant eastward contribution in this regime, as was also found by McLandress et al. (2006). Indeed, if we plot only the quasi-geostrophic contribution from the PW EPF divergence, the HIAMCM yields the signature that is typical for the westward propagating PWs in the summer MLT (see also Becker et al., 2022, their Figure 5).

The HIAMCM exhibits a reversed residual circulation in the summer lower thermosphere centered around 10^{-4} hPa ($z \sim 110$ km) (Figures 3a and 3b), with the poleward branch of this circulation around 3×10^{-5} hPa being driven by westward EPF divergence from both PWs and GWs (Figure 4). While the westward PW EPF divergence in this regime is due mainly to thermal tides (Becker, 2017), the westward GW drag in the summer lower thermosphere is presumably due to secondary GWs that are generated in the regime of the eastward primary GW drag in the mesosphere below. The generation mechanism of such secondary GWs would be analogous to the aforementioned MSVC in the winter atmosphere. Figures 3a and 3b furthermore show that the reversed residual circulation in the summer lower thermosphere is more pronounced during the SSW when compared to the strong vortex period. A closer inspection of the model data showed that this difference is caused by a stronger westward PW EPF divergence, which in turn is likely caused by stronger thermal tides generated in the lower and middle atmosphere during this later phase of the season. Note that a reversed residual circulation in the lower thermosphere is also found in other models (e.g., McLandress et al., 2006; Smith et al., 2011), albeit with different meridional extents in different models.

Figure 4 lends further support to the interpretation given above regarding the changes of the zonal-mean circulation during the SSW 2017. The winter mesospheric GW drag changes from strongly westward in late December to eastward during the wind reversal, causing the mesospheric cooling via a corresponding anomaly of the winter-mesospheric branch of the residual circulation. The westward and eastward GW drag during these phases of the winter season is due to primary GWs with mainly tropospheric origin (primary GWs can also be generated by the polar vortex).

The situation is different at higher altitudes. In the winter upper MLT, the dissipation of secondary GWs generates an eastward drag before the SSW. When comparing the period from 11 December 2016 to 8 January 2017 to the period from 9 to 25 January 2017 in Figure 2b, we can conclude that this eastward GW drag is stronger when the polar vortex is stronger. This is consistent with former model results that showed stronger secondary GWs in the southern winter MLT than in the northern winter MLT (Avsarkisov et al., 2022; Becker et al., 2020). Vadas and Becker (2019) argued that MSVC is stronger when the primary GWs propagate to higher altitudes before they break. Indeed, the primary westward GW drag is stronger in amplitude (and located at higher altitudes) for a stronger polar vortex (e.g., Karlsson & Becker, 2016, their Figure 2, see also Figure 2b in the present study). Also note that if the eastward GW drag in the winter mesopause region was due to primary GWs generated in the troposphere with fast enough phase speeds to exceed critical level absorption in the stratosphere, their effect should be weaker when the polar vortex is stronger. These arguments are consistent with the fact that nudged models with parameterized GWs show better fidelity in simulating the winter MLT when the polar vortex is perturbed than when the vortex is stable and strong (Harvey et al., 2022). The reason is that the neglect of secondary GWs in these models is most significant in the latter case.

Figures 2b, 4c, and 4d show that the primary westward GW drag in late December is much stronger and located at a lower altitude than the primary eastward GW drag maximum during the wind reversal around 31 January. Even though secondary GWs are likely also generated in the regime of the eastward primary GW drag during the wind reversal, their amplitudes are likely much weaker than those of the secondary GWs in late December because of the aforementioned dependence on the primary GW amplitudes. This reasoning is confirmed when we compare the GW drag (GW EPF divergence) in the winter lower thermosphere for the two time periods. While there is a pronounced maximum of the secondary eastward GW drag from about 3×10^{-4} to 3×10^{-6} hPa (about 100–170 km) in Figure 4c (strong vortex), there is only some weak eastward and westward GW drag in this region in Figure 4d (SSW).

The reduced wave driving by secondary GWs in the winter lower thermosphere during the SSW translates to higher altitudes. The GW EPF divergence in Figure 4c (strong polar vortex) is strongly eastward above 10^{-6} hPa ($z \sim 200$ km) at middle to high latitudes, but is much weaker in Figure 4d (during the SSW). As argued in Vadas and Becker (2019), Becker and Vadas (2020), and Becker et al. (2022), GW effects at these altitudes in the winter thermosphere are due mainly to higher-order GWs. Hence, reduced MSVC is the likely reason for the weakening of thermospheric GW effects during and after the SSW. For the present model setup, we find a strong eastward GW drag in the winter thermosphere during a strong polar vortex instead of a westward drag as was found in Becker et al. (2022). This difference is caused by the auroral circulation that is now included in the HIAMCM, as will be discussed in more detail in Section 5.

Another difference in the current model version when compared to the former HIAMCM results is found in the lower thermosphere over the polar caps. Here, the current model generates a pronounced eastward PW EPF divergence. This feature is absent when the auroral circulation is not accounted for (see Becker et al. (2022, Figures 5a and 5b) or Becker and Vadas (2020, Figure 2a)). We calculated the EPF divergence from the diurnal tide and found mainly the same eastward EPF divergence above about 3×10^{-5} hPa ($z \sim 140$ km) at high latitudes during strong vortex and SSW periods as in Figures 4a and 4b (not shown). Hence, we verified that the eastward PW EPF divergence in the polar thermosphere is due to the diurnal tide. The reason for this effect is that the auroral circulation corresponds to a strong forcing of horizontally rotational flow of the migrating diurnal tide in the polar regions. This is analogous to the EPF divergence of Rossby waves in the troposphere (Edmon et al., 1980). More specifically, Rossby waves are generated at middle to high latitudes in the lower troposphere, and this region is characterized by a significant eastward EPF divergence (opposite to the intrinsic phase propagation direction). The westward EPF divergence from Rossby waves due to wave dissipation is then found at higher altitudes, that is, in the upper troposphere and in the winter stratosphere. We argue that the regions where horizontally rotational flow of migrating tides is generated must also be characterized by an eastward EPF divergence, while the dissipation of tides gives rise to westward EPF divergence (Becker, 2017).

Summarizing, our zonal-mean results for the winter 2016/2017 from the nudged HIAMCM are largely consistent with the well-known dynamics in the middle atmosphere during a strong polar vortex and an SSW event. Differences to former model studies are found regarding the significant roles of secondary and higher-order GWs in the winter upper mesosphere and thermosphere, because these waves are not simulated in conventional models due to the limitations of current GW parameterizations (see discussions in Becker & Vadas, 2020; Bölöni et al., 2021). Therefore, our new model results lend confidence to study the difference in the MSVC during late December 2016 (when the polar vortex is strong) and the SSW in 2017 with regard to the resolved GWs in the thermosphere (Section 5), and to compare the simulated GW perturbations in the winter thermosphere to observed TEC perturbations (Section 6).

5. GW Response in the Thermosphere During the SSW in 2017

Before considering the MSVC during the SSW in late January/early February 2017, we first show the winds and GW perturbations in late December 2016. We use the same wavenumber decomposition as for the EPF divergence to distinguish between the large-scale flow and GWs (Section 2). Figure 5 shows longitude-height plots at 60°N of the temperature perturbation (left column) and the large-scale horizontal wind components (right column, zonal wind by colors, meridional wind by black contours) on 27 December 2016 at 12:00 (upper row) and 19:30 UT (lower row). Note that 60°N corresponds to the latitude regime where the GW drag in the winter middle atmosphere is westward (eastward) when the polar vortex is strong (during the SSW).

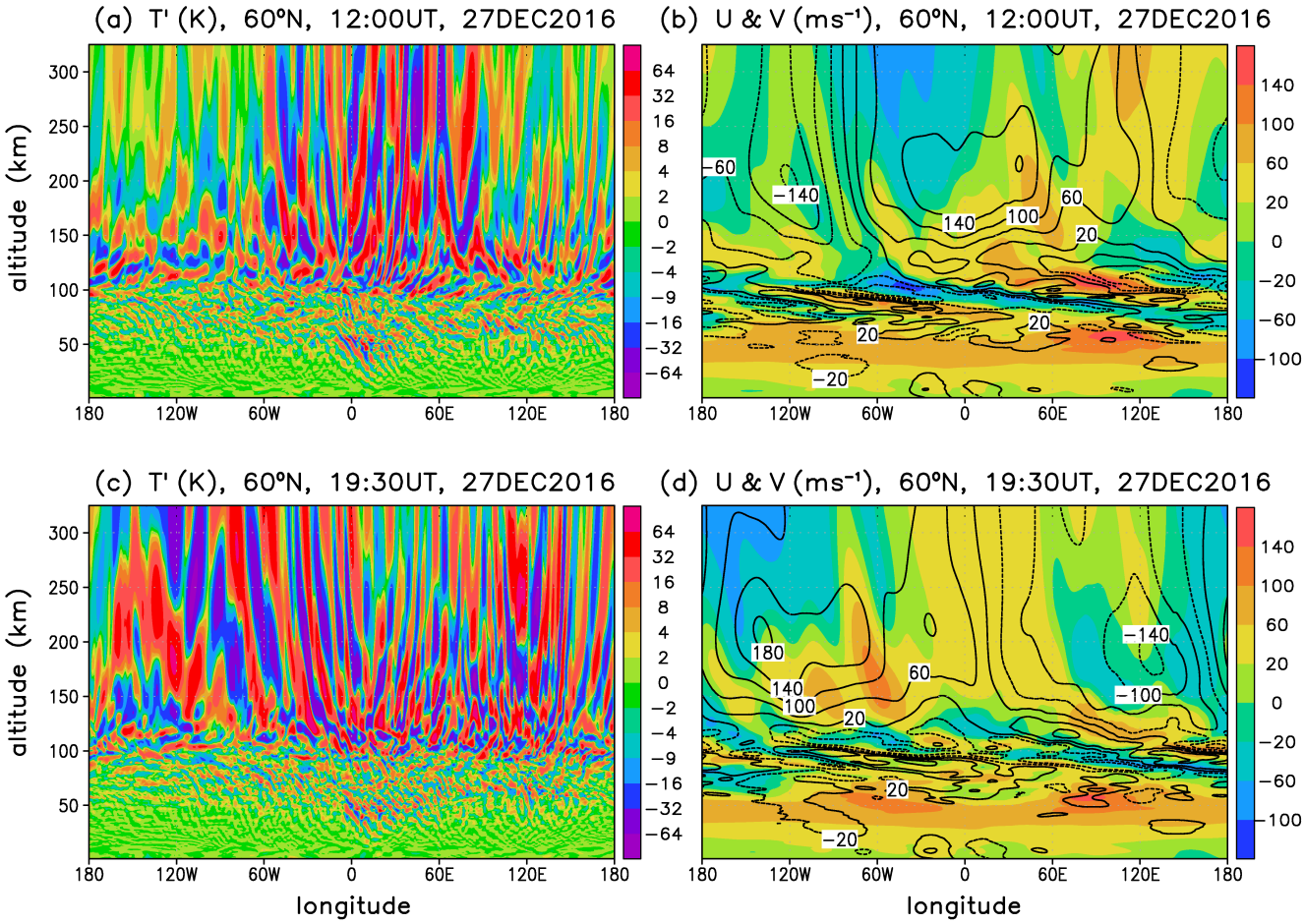

Figure 5. (a) Longitude-height plot of gravity wave (GW) temperature perturbations at 60°N on 27 December 2016 at 12:00 UT. (b) Large-scale zonal wind (colors) and meridional wind (black contours for ±20, ±60, ±100, ±140, … m s^{-1}). (c) Same as (a), but at 19:30 UT. (d) Same as (b), but at 19:30 UT. See Section 2 for the definition of GW perturbations and the large-scale flow.

Figure 5a indicates strong primary GWs in the stratosphere and lower mesosphere over northern Europe (from about 10°W to 20°E). The phase inclination of these GWs is indicative of westward propagation relative to the mean flow. The flattening of the GW phases in the mesosphere over Europe indicates dynamical instability and subsequent dissipation induced by turbulent diffusion, leading to GW-mean flow interaction (GW drag and energy deposition). This process is induced by the Doppler shifting of the westward GWs toward smaller intrinsic frequencies (shorter vertical wavelengths) caused by westward vertical wind shear (see colors in Figure 5b). Similar features as over Europe are seen in other longitude bands in Figure 5a, for example, from about 90 to 110°E and from about 140 to 160°E.

Since the GW-mean flow interactions are intermittent and localized in space, secondary GWs are generated from the resulting imbalances of the mean flow (e.g., Vadas et al., 2018). Figure 5a suggests that secondary GWs become the predominant GWs in the winter mid and upper mesosphere (for $z \sim$ 70–100 km). The phase inclinations of these GWs are indicative of both westward and eastward propagation directions, with eastward propagation prevailing with increasing altitude because of negative vertical shear of the large-scale zonal wind (colors in Figure 5b). This is visible in the mesopause region from about 10 to 40°E and from about 90 to 150°E. When the secondary GWs propagate into the mesopause region and lower thermosphere, they become subject to strong refraction caused by the variable large-scale vertical wind shears (Figure 5b). These wind shears are due to the semi-diurnal tide and traveling PWs. The secondary GWs dissipate in this regime, which can be concluded from Figure 5a since many of the GW phase lines flatten or become more horizontal with increasing height in the mesopause region and lower thermosphere. Again, the resulting wave-mean flow interactions are intermittent and localized in space, giving rise to the generation of tertiary GWs. Overall, there are mainly higher-order GWs

above about 150 km. These waves have very long vertical wavelengths and phase speeds of several 100 m s^{-1} (Becker & Vadas, 2020; Vadas, 2007; Vadas & Becker, 2019), which is much larger than what is typical in the lower and middle atmosphere. Their phase inclinations in Figure 5a do not indicate clear westward or eastward propagation directions, especially not in the longitude sector from about 30°W to 60°E.

When we consider the same snapshots 7.5 hr later (at 19:30 UT, second row in Figure 5), the picture is very similar to that at 12:00 UT up to about 80 km height. Above ∼80 km, however, the large-scale wind patterns have migrated to the west (compare Figures 5b and 5d). In the thermosphere above ∼150 km, these wind patterns are governed by the in situ-generated diurnal tide. When comparing the colors and contours in the wind plots in Figures 5b and 5d, we can see that the large-scale wind in the thermosphere is mainly poleward over Europe at 12:00 UT, but has rotated to being mainly eastward at 19.30 UT. Consistent with the notion that medium-scale GWs at F-region altitudes propagate roughly against the mean winds associated with the diurnal tide, the GWs with the largest amplitudes at 19:30 UT above ∼200 km show a clear westward propagation component from about 50 to 10°W.

Figures 6a and 6b show NH polar projections of GWs (colors) and the polar vortex (in terms of the geometric height at pressure surfaces, white contours) on 27 December 2016 at 12:00 UT. From Figure 6a we can infer a strong stratospheric polar vortex that is centered over Spitsbergen. Furthermore, there is a pronounced GW packet from the North Sea to Finland, which could have been emitted by the upper tropospheric jet or by the polar vortex. Additional significant GW activity in the stratosphere in Figure 6a can be seen from the Caspian Sea to northeastern Siberia. The mesosphere (at 0.01 hPa, Figure 6b) shows high variability of the instantaneous height contours caused by GWs. Furthermore, we can infer from Figure 6b that the GW activity spreads out horizontally from the stratosphere to the mesosphere. It is likely that secondary GWs give the major contributions to the temperature perturbations at 0.01 hPa.

Depending on the wind shear associated with the large-scale tidal winds, both eastward and (to a lesser extent) westward propagating secondary GWs can propagate into the mesopause region where they dissipate, which gives rise to the generation of higher-order GWs that propagate to higher altitudes into the thermosphere. Figures 6c and 6e show the GWs (colors) and large-scale winds (white arrows) at 12:00 and 19:30 UT, respectively. The altitude in these panels is 150 km height, which is somewhat above the assumed sources of the higher-order GWs. Since these GWs have not yet been subject to strong directional dissipation induced by the large-scale tidal winds, we see concentric ring structures which are indicators of GW sources in the lower thermosphere. Figure 6e shows two such regions: Over the Scandinavia (also visible in Figure 6c) and over eastern Siberia. The approximate centers of these concentric ring structures are indicated by two additional black arrows in Figure 6e. The higher-order GWs from both sources have significant amplitudes also at 250 km. Due to the strong poleward winds from the diurnal tide over the European sector at 12:00 UT, the equatorward propagating waves are most prominent in Figure 6d, with some GW activity also propagating eastward over eastern Europe and westward over the Atlantic. There are hardly any GWs propagating poleward at 250 km over the European sector at 12 UT because this portion of the concentric ring structure dissipated between 150 and 250 km. At 19:30 UT (Figure 6f), however, the wind-induced directional dissipation of GWs from the source over the Norwegian Sea favors westward GW propagation over the western North Atlantic and southward propagation over northeastern Canada at 250 km, while the GW amplitudes over Europe have weakened. The situation is different for the concentric ring structure over Siberia in Figures 6e and 6f. Here, the large-scale tidal winds are weaker and mainly equatorward. Hence, the effect of wind-induced directional dissipation between 150 and 250 km height weakens those GW components with equatorward propagation direction. Overall, the second and third row in Figure 6 illustrate the dramatic dependence of the thermospheric (higher-order) GWs on the diurnal tide.

We now consider the situation during the SSW. Figure 7 shows GW perturbations and large-scale winds analogous to Figure 5, but on 31 January 2017. We pick 31 January because this is the day of maximum wind reversal in the stratosphere (Figure 1). The wind reversal is indicated in Figures 7b and 7d by the predominantly westward flow in the upper stratosphere and lower mesosphere. Figures 7a and 7c show westward and eastward propagating primary GWs in the stratosphere. The phase inclinations of these GWs in the mesosphere indicate predominantly eastward propagation, as is expected due to the predominantly westward direction of the large-scale zonal wind. The GWs in the stratosphere and mesosphere during the wind reversal have much weaker amplitudes than during the strong vortex period (compare Figure 7a to Figure 5a, also note that we use the same color bars and contours in Figures 5 and 7). These predominantly eastward propagating primary GWs dissipate in the upper

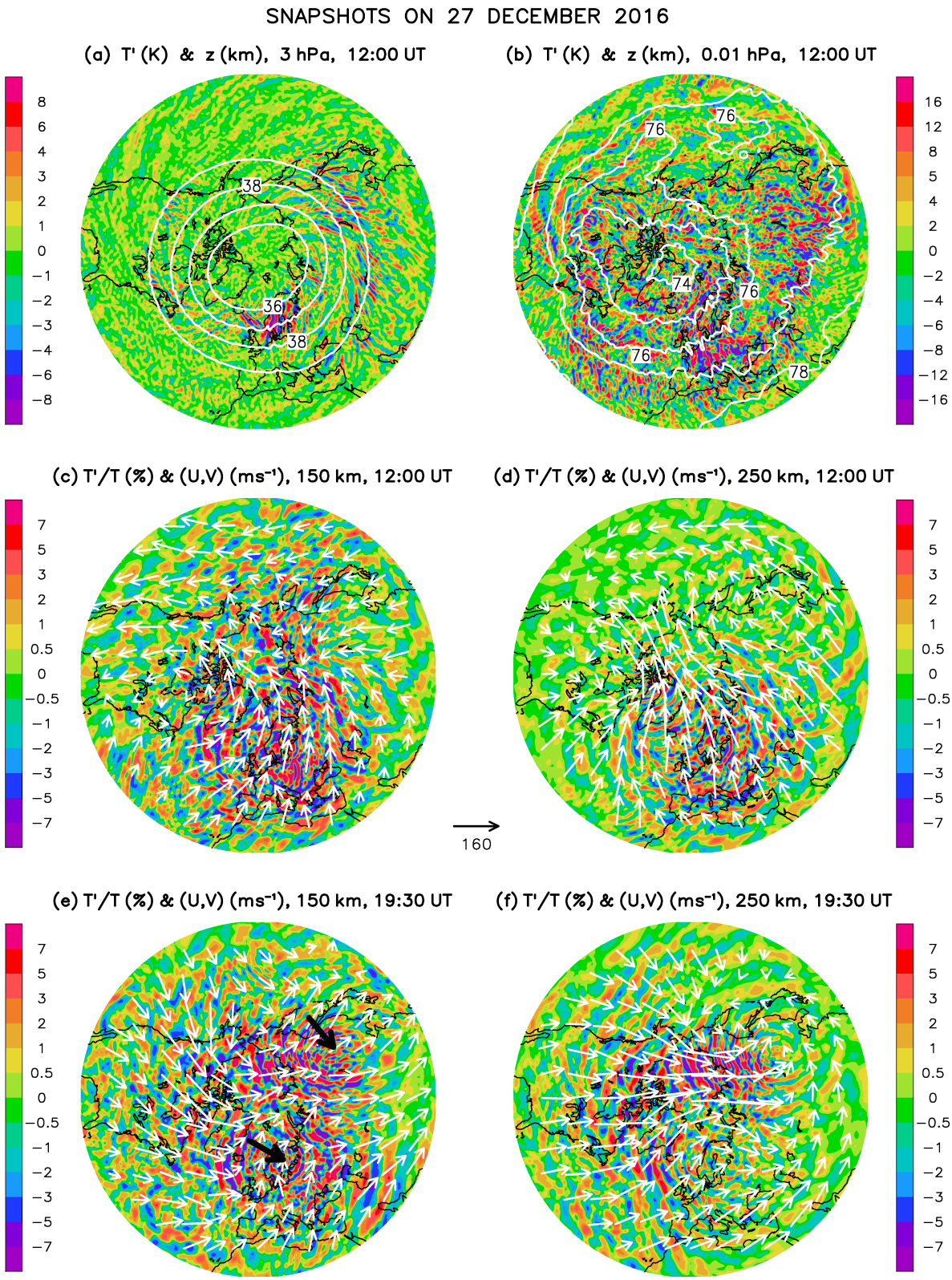

Figure 6. (a) North polar plot of gravity wave (GW) temperature perturbations (colors) and geometric height (white contours, interval 1 km) at 1 hPa on 27 December 2016 (12:00 UT). (b) Same as (a) but at 0.01 hPa using a different color scale. (c) Northpolar plot of relative temperature GW perturbations (colors) and the large-scale horizontal wind (white arrows, arrow scale in m s^{-1} given between panels (c) and (d)) at 150 km height on 27 December 2016 (12:00 UT). (d) Same as (c) but at 250 km height. (e, f) Same as (c, d), but at 19:30 UT on 27 December 2016. The Greenwich meridian is oriented toward the bottom in each panel and the equatorward edge is 25°N. The approximate centers of two concentric ring structures are indicated by additional black arrows in panel (e).

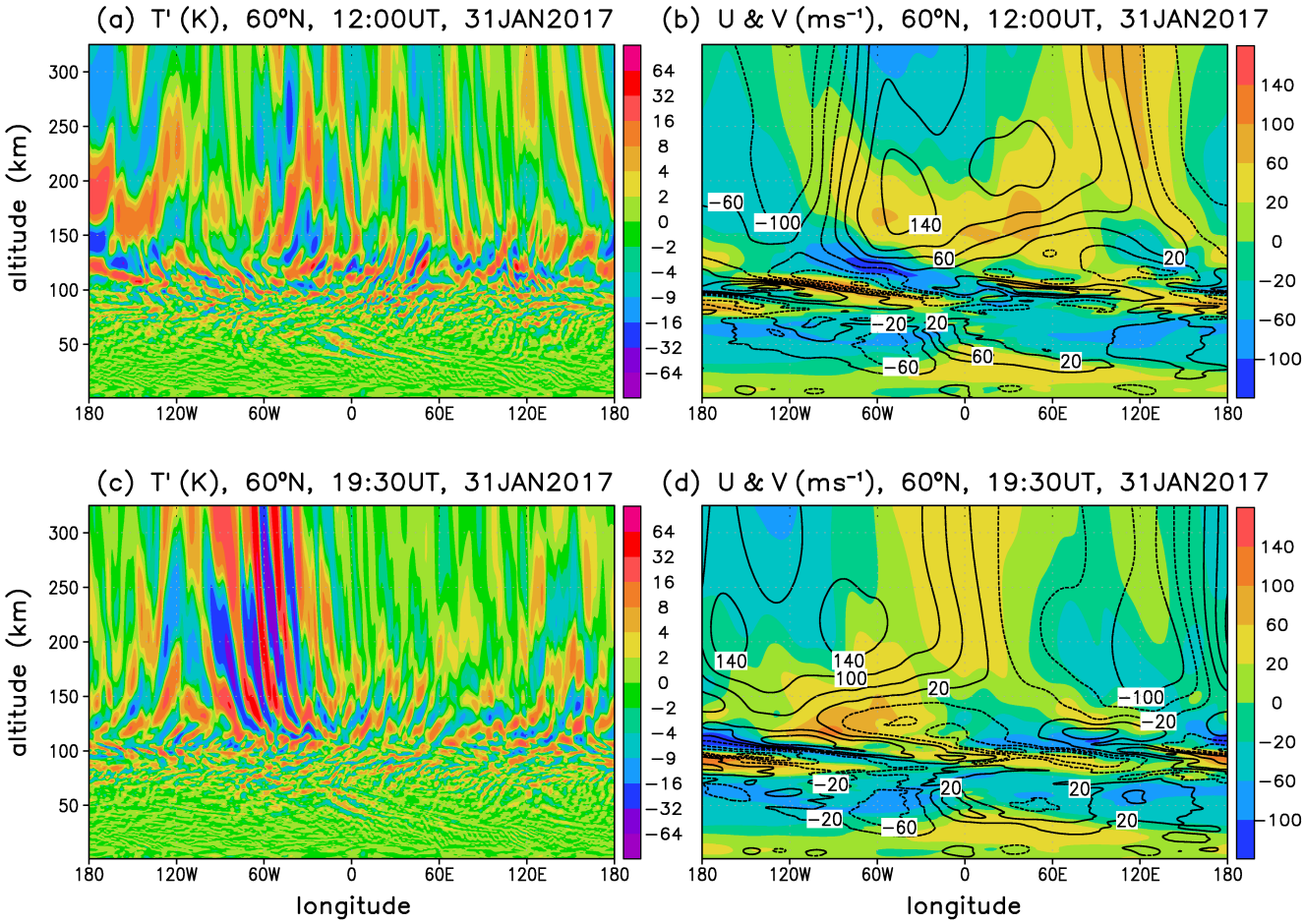

Figure 7. Same as Figure 5, but on 31 January 2017.

mesosphere due to eastward vertical wind shear, giving rise to the eastward primary GW drag during the wind reversal (Figures 2b and 4d). Since this process is intermittent and localized in space, broad spectra of secondary GWs are generated, which propagate to higher altitudes. The phase inclinations of these secondary GWs indicate eastward and westward propagation directions in the mesopause region and lower thermosphere, giving rise to very weak zonal GW drag in the zonal mean when these secondary GWs dissipate in the lower thermosphere (see Figure 4d). Like on 27 December, higher-order GWs are generated in the lower thermosphere. Only those higher-order GWs with large intrinsic horizontal phase speeds (large vertical wavelengths) can propagate to high altitudes in the thermosphere (Vadas, 2007).

As a particular feature of higher-order GW generation visible in Figure 7a, we mention a pronounced source at about 100 km height and 50–30°W. The GW phases that emerge from this region show eastward (westward) propagation somewhat farther to the east (west). At 12:00 UT, these GWs dissipate at about 120–130 km height. Figure 7b shows that this dissipation is induced by the tidal winds at this time, showing eastward (westward) vertical wind shear to the east (west) from this GW source. At 19:30 UT, however, the tidal winds have advanced to the west (Figure 7d) such that westward propagating GWs from the aforementioned GW source can propagate to higher altitudes in the thermosphere. This is suggested by the large GW amplitudes in Figure 7c from about 100 to 30°W. In the longitude sector around 60°W, these GWs should also have a strong southward component, as is suggested by the poleward wind (contours in Figure 7d).

Figure 8 shows GW perturbations and large-scale winds on 31 January 2017 analogous to Figure 6, using the same color bars, contour intervals, and arrow scale. Figure 8a reveals a small and displaced polar vortex centered over the North Atlantic between Scotland and Iceland. A large-amplitude inertia GW packet is visible from the Baltic Sea to northern Greenland. This packet is presumably generated in the stratosphere by the weak and

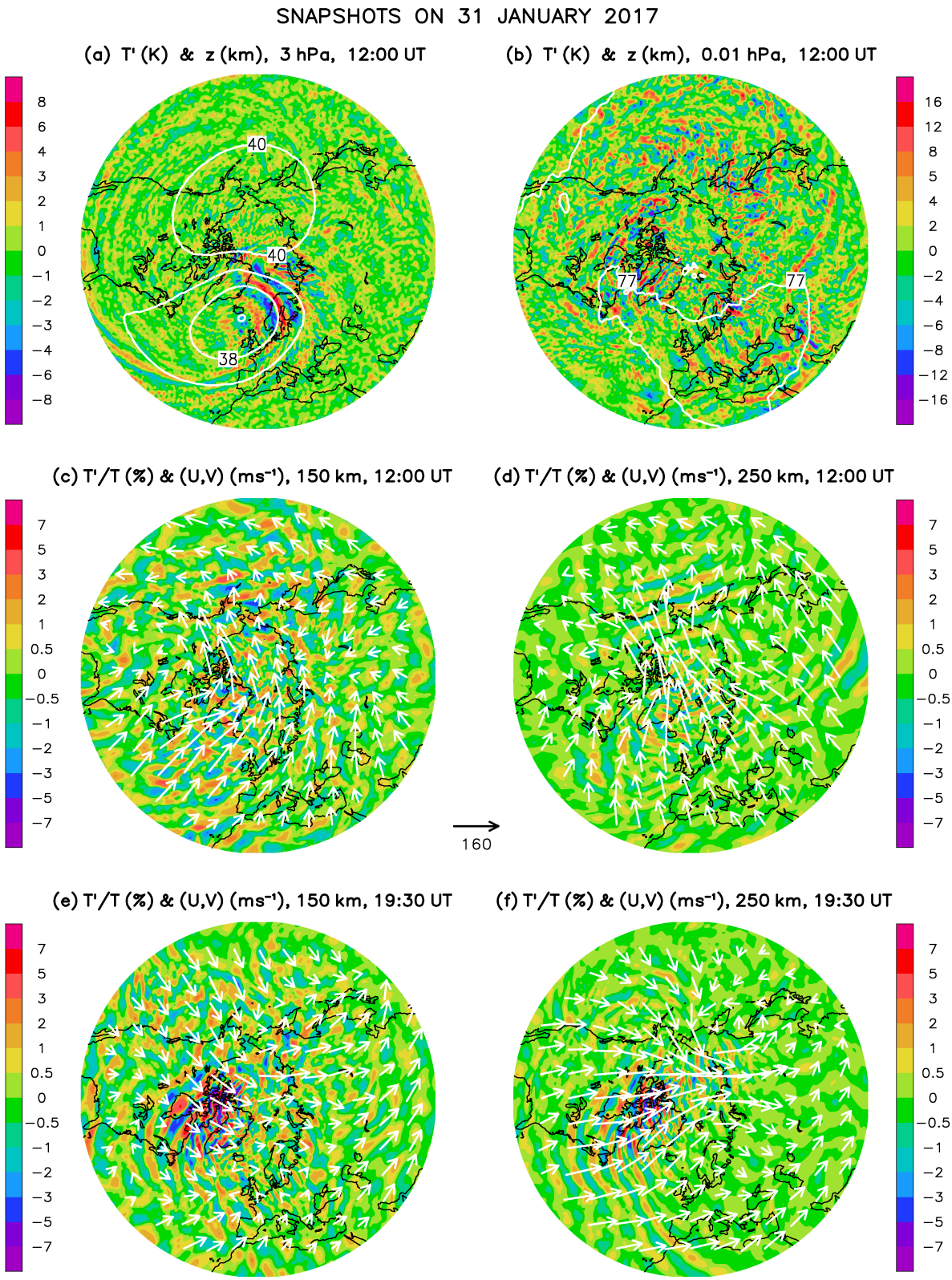

Figure 8. Same as Figure 7, but on 31 January 2017.

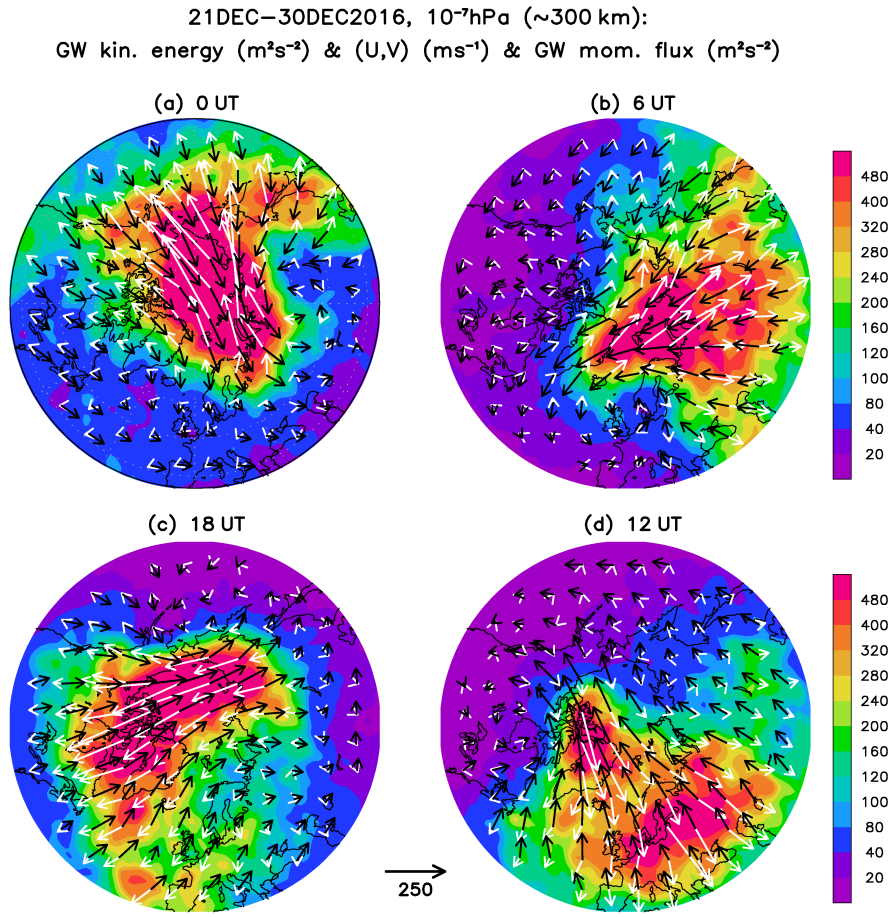

Figure 9. Average daily cycle of gravity wave (GW) effects in the thermosphere during the strong vortex period from 21 to 30 December 2016 at 10^{-7} hPa ($z \sim 300$ km). Colors show the average GW kinetic energy per unit mass at (a) 00:00, (b) 06:00, (c) 18:00, and (d) 12:00 UT. The black arrows show the average large-scale horizontal wind during these universal times, while the white arrows show the corresponding vertical flux of horizontal momentum due to GWs. The arrow scale (between panels (c) and (d)) is the same for the black and white arrows, but refers to the respective units, that is m s^{-1} or m^2 s^{-2}. The Greenwich meridian is oriented toward the bottom in each panel and the equatorward edge is 35°N.

displaced polar vortex. Compared to the strong vortex case in Figure 6, the GWs in Figure 8 have much weaker amplitudes at all altitudes. This is particularly the case for the southward propagating GWs over Europe at 250 km and 12:00 UT (Figure 8d). The imprint of the GW source in the MLT at about 60°N and 40°W that we deduced from Figure 7c is not visible at 150 and 250 km and 12:00 UT in Figures 8c and 8d, but is clearly visible 7.5 hr later in Figures 8e and 8f, as is expected from our discussion of Figure 7c. Figures 8e and 8f also show partial concentric ring structures from northeastern Canada to Greenland. This indicates that these GWs are indeed generated by localized and intermittent body forces (e.g., Vadas et al., 2018), and are subject to wind-induced directional dissipation above their sources. Figures 8e and 8f further suggest there are several GW sources in this region. The overall picture at 19:30 UT and 250 km (Figure 8f) is characterized by westward to southward propagating GWs from Greenland to the northeastern United States and Canada.

In the remainder of this section, we further quantify the daily cycle of GW effects in the thermosphere during the strong vortex period and the SSW. For this purpose, we post-processed the model data from 21 to 30 December 2016, and we then computed the averages from 23:30 to 00:30, 05:30 to 06:30, 11:30 to 12:30, and 17:30 to 18:30 UT, taking all 10 days into account and taking advantage of the 10 min cadence of the model output. Figure 9 illustrates the resulting average daily cycle in the thermosphere at 10^{-7} hPa ($z \sim 300$ km) for the strong-vortex period at 00:00, 06:00, 12:00, and 18:00 UT. Colors show the GW kinetic energy per unit mass. The black arrows show the large-scale horizontal wind, while the white arrow show the vertical flux of horizontal momentum due to GWs (hereafter: momentum flux). The arrow scale is inserted at the bottom between Figurs 9c and 9d, and is

the same for the black and white arrows in the respective units. The black arrows confirm the daily cycle of the large-scale horizontal wind in the thermosphere that is due to the diurnal tide, with cross-polar flow from the dayside to the nightside, which facilitates equatorward propagation of higher-order GWs during local noon and afternoon (Becker & Vadas, 2020; Crowley & Rodrigues, 2012). This GW propagation direction against the tidal flow is evident also from the average picture of Figure 9, because the momentum flux vectors (white arrows) are roughly opposite to the large-scale wind (black arrows).

The results shown in Figure 9 go beyond our previous estimates by revealing a significant daily cycle of the GW amplitudes in the winter thermosphere. Indeed, on average, the GW amplitudes at middle latitudes in the winter thermosphere around 300 km are strongest when the tidal flow is strongest, which is the case roughly around local time noon and afternoon when the tidal flow has a strong poleward component and the GW momentum flux is roughly equatorward. Furthermore, the GW amplitude maximum extends northwestward, that is, to polar latitudes when the local time is in the morning hours. In this region the tidal wind has a strong westward component such that the GWs in this regime exhibit a strong eastward momentum flux. This effect is induced in the HIAMCM by the auroral circulation that is forced by the simple ion drag parameterization over the polar caps as mentioned in Section 2 and described in Appendix A. More specifically, the additional ion drag forces a strong horizontally rotational flow across the pole, and this flow is shifted somewhat into the dawn sector (Forbes, 2007). As a result, there is a strong westward flow poleward of about 70°N at dawn. It is because of this westward flow that the GW drag shows a significant eastward component in the thermosphere in the zonal mean (Figure 4c).

Note that there is a strong cancellation of the GW momentum flux and drag contributions from different longitudes in the zonal and temporal mean because of the variations of GW propagation and dissipation induced by the tidal winds. Given this highly dynamical picture, a zonal-mean zonal GW drag obscures most of the information about the actual GW-mean flow interactions. Indeed, GW-mean flow interaction in the winter thermosphere is mainly due to GW-tidal interaction. The crucial role of the tides in controlling GW instability and mean flow effects is also well known for the MLT (e.g., Becker, 2017; Becker & Vadas, 2018; Heale et al., 2022; Liu et al., 2014; Ortland & Alexander, 2006; Senf & Achatz, 2011). It is beyond the scope of this paper to explore the GW-tidal interactions in the thermosphere in greater detail.

Figure 10 shows the average daily cycle during the SSW (from 26 January to 4 February 2017). Consistent with the above discussion when comparing snapshots on 27 December and 31 January, the GW amplitudes and momentum fluxes are much weaker at all longitudes at middle and polar latitudes when compared to the strong-vortex period (Figure 9). Nevertheless, the general behavior found for the strong-vortex period is also reflected in Figure 10. A specific feature during the strong-vortex period is that the equatorward propagating GWs over the European sector from about 40 to 60°N during noon and afternoon (Figure 9d) have stronger amplitudes than the corresponding GWs over North America and the western North Atlantic (Figure 9c). This relative regional difference is reversed during the SSW (Figures 10c and 10d). Also the snapshots in Figures 6d, 6f, 8d, and 8f reflect these opposite relative regional differences during the strong-vortex period and the SSW.

Summarizing, our model results show that the SSW has a substantial weakening effect on the amplitudes of the higher-order GWs in the thermosphere. In addition, we find regional differences of this effect. Such differences may depend on how the polar vortex is disrupted and/or displaced during the SSW, that is, different geographical distributions of the GW weakening effect in the thermosphere may be observed for different vortex geometries associated with SSW events.

6. Comparison of Simulated GWs and Observed TEC Perturbations

We now inspect keograms of the GWs in the thermosphere and compare these with the TEC perturbations from ground-based measurements over Europe and over North America as described in Section 3. Figure 11 compares keograms of simulated relative temperature perturbations at 300 km height over Europe on 27 December 2016 with TEC perturbations (dTEC) from the same day. The time-longitude and time-latitude plots from the model (upper panels) confirm the change of the propagation directions of the GWs at middle latitudes with local time, namely from eastward in the morning to southward around noon and early afternoon, and to westward in the evening. The same behavior is also indicated by the dTEC (lower row in Figure 11). Most importantly, the simulated scales and propagation characteristics of the simulated GWs bear a strong similarity to those of the corresponding dTEC. Note that this comparison is only of qualitative nature in the sense that we cannot predict the

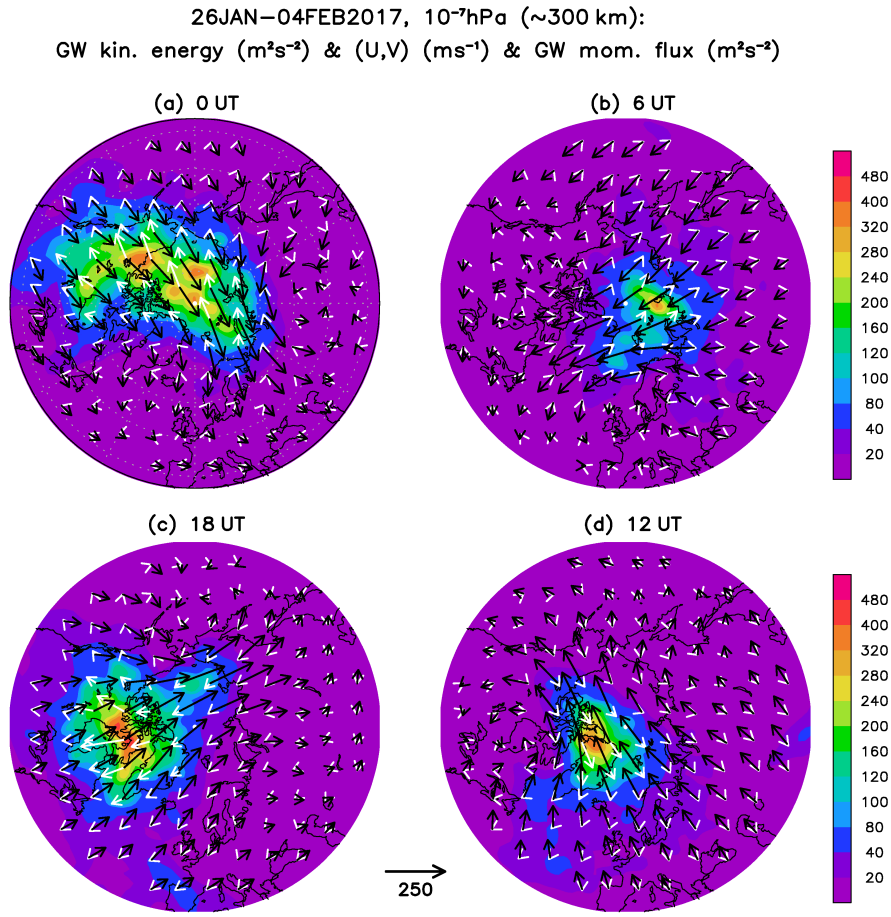

Figure 10. Same as Figure 9, but for the period of the sudden stratospheric warming from 26 January to 4 February 2017. Note that the same color and vector scales are used as in Figure 9.

TEC perturbation amplitude from the model in its current configuration. However, since the single-ion approximation is valid at about $z \geq 200$ km, the horizontal wavelengths and periods of the TIDs will mirror those of the underlying GWs (Nicolls et al., 2014; Vadas & Nicolls, 2009). Hence, Figure 11 strongly suggests that the observed dTEC are dynamically induced from below due to MSVC, leading to higher-order GWs in the thermosphere and corresponding perturbations in the plasma due to advection of the O^+ ions by the neutral wind perturbations projected onto the magnetic field lines (Nicolls et al., 2014). Figures 11a, 11b, and 11d include a few straight white lines to indicate the propagation of the wave phases. For case #1 (local time noon), these phase lines correspond to a horizontal wavelength of ~700 km and a period of ~45 min, resulting in an equatorward horizontal phase speed of $c_{ph} \sim 270$ m s^{-1}. The case #2 GW phases in Figure 11b shortly after nightfall have an approximate southwestward propagation direction and a period of ~60 min. The apparent horizontal wavelengths in longitudinal and latitudinal directions are about 800 and 900 km, respectively, yielding a true horizontal wavelength of about 450 km and a phase speed of $c_{ph} \sim 130$ m s^{-1}. Such values are typically observed for medium-to-large-scale TIDs, even though the simulated wavelengths are somewhat larger than found by of Frissell et al. (2016).

Figure 12 shows a comparison analogous to Figure 11, but over North America on 27 December 2016. We observe qualitatively the same behavior as over Europe, with similar scales and propagation characteristics of the GWs and dTEC. Also note that the keograms in the upper panels of Figures 11 and 12 indicate somewhat weaker GW amplitudes over North America than over Europe. This is consistent with our findings from the previous section (see Figure 9). The lower panels in the two figures suggest that this regional difference is also reflected in the dTEC, with weaker dTEC over North America than over Europe during the strong-vortex period (except for

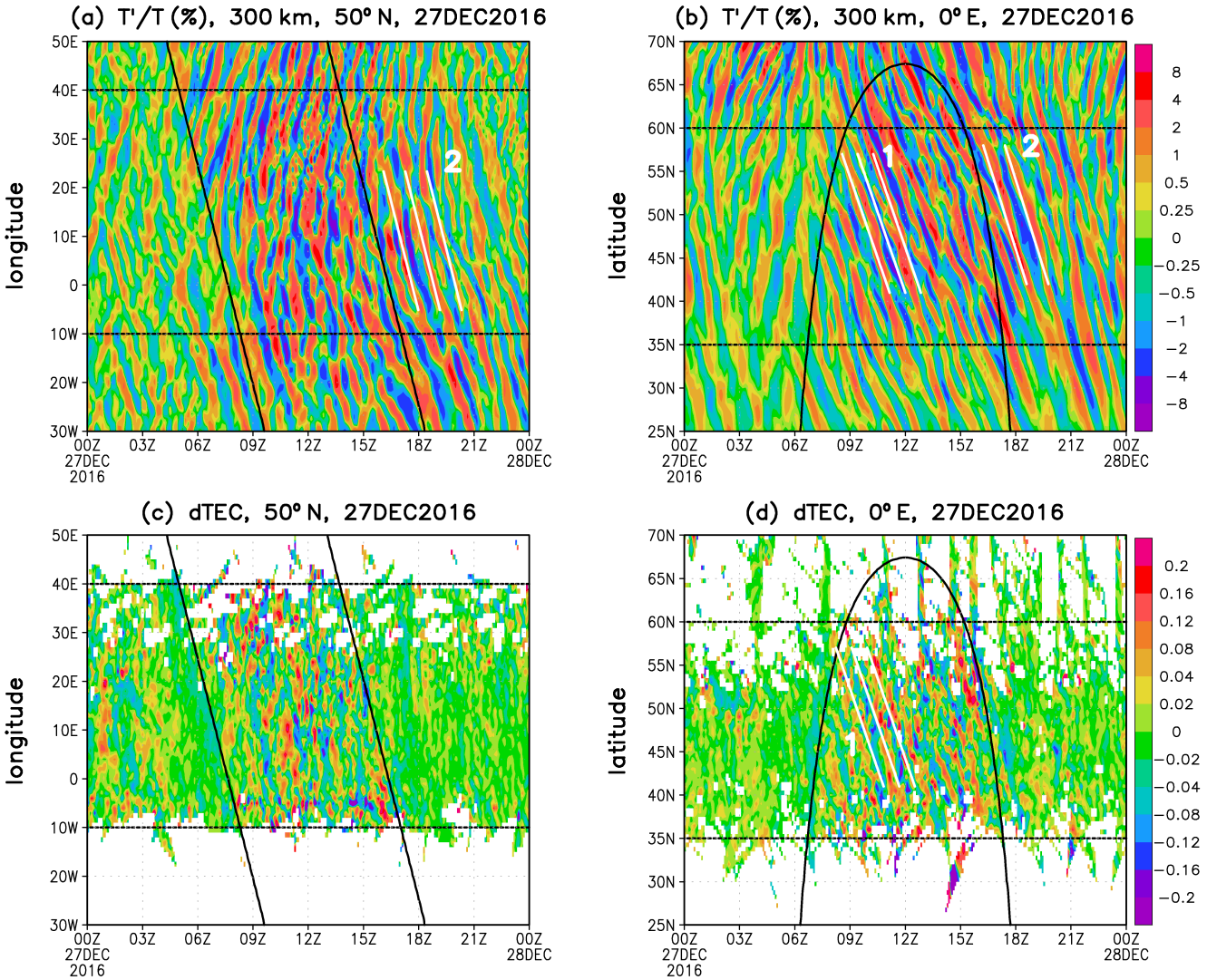

Figure 11. Keograms of simulated gravity waves and observed differential TEC (dTEC) on 27 December 2016 over Europe. Upper row: Relative temperature perturbations at 300 km height and 50°N from 30°W to 50°E (panel (a)), and at 0°E from 25 to 70°N (panel (b)). Lower row: Same as upper row, but for the dTEC. The black horizontal lines mark 10°W and 40°E (left), and 35 and 60°N (right). These lines are included to facilitate the comparison of the upper and lower panels. Sunrise and sunset are indicate by slanted (left) and curved (right) black lines. Some wave phases are indicated by additional white lines (see text for further details).

latitudes south of 35°N where no data are available in Figure 11d). This adds further confidence to our hypothesis that the observed dTEC are caused by MSVC.

Figures 13 and 14 show keograms analogous to Figures 11 and 12, respectively, but on 30 January 2017, that is, during the wind reversal in the winter middle atmosphere. We did not pick a later day during the wind reversal because of the increased geomagnetic activity from 31 January to 6 February in 2017 (when geomagnetic activity was Kp = 3+ to Kp = 5, see Section 3) in order to compare the model results only with dTEC that are most likely caused by GWs from below. Consistent with the results from the previous section, we find that the GWs are much weaker over Europe during the SSW as compared to the strong-vortex period (compare the upper panels in Figure 13 with those in Figure 11). There is also some weakening over North America (compare the upper panels in Figures 14 and 12), but the effect is weaker in this region than over Europe. As a result, there is stronger GW activity over the North America than over Europe during the SSW, which is also consistent with Figure 10. The keograms computed from the dTEC over North America on 30 January 2017 also show some weakening during the SSW as compared to 27 December 2016, but the weakening effect in this region appears to be weaker than the weakening effect over Europe. Note the large-amplitude TID at 16:00–17:00 UT in Figure 14c that is

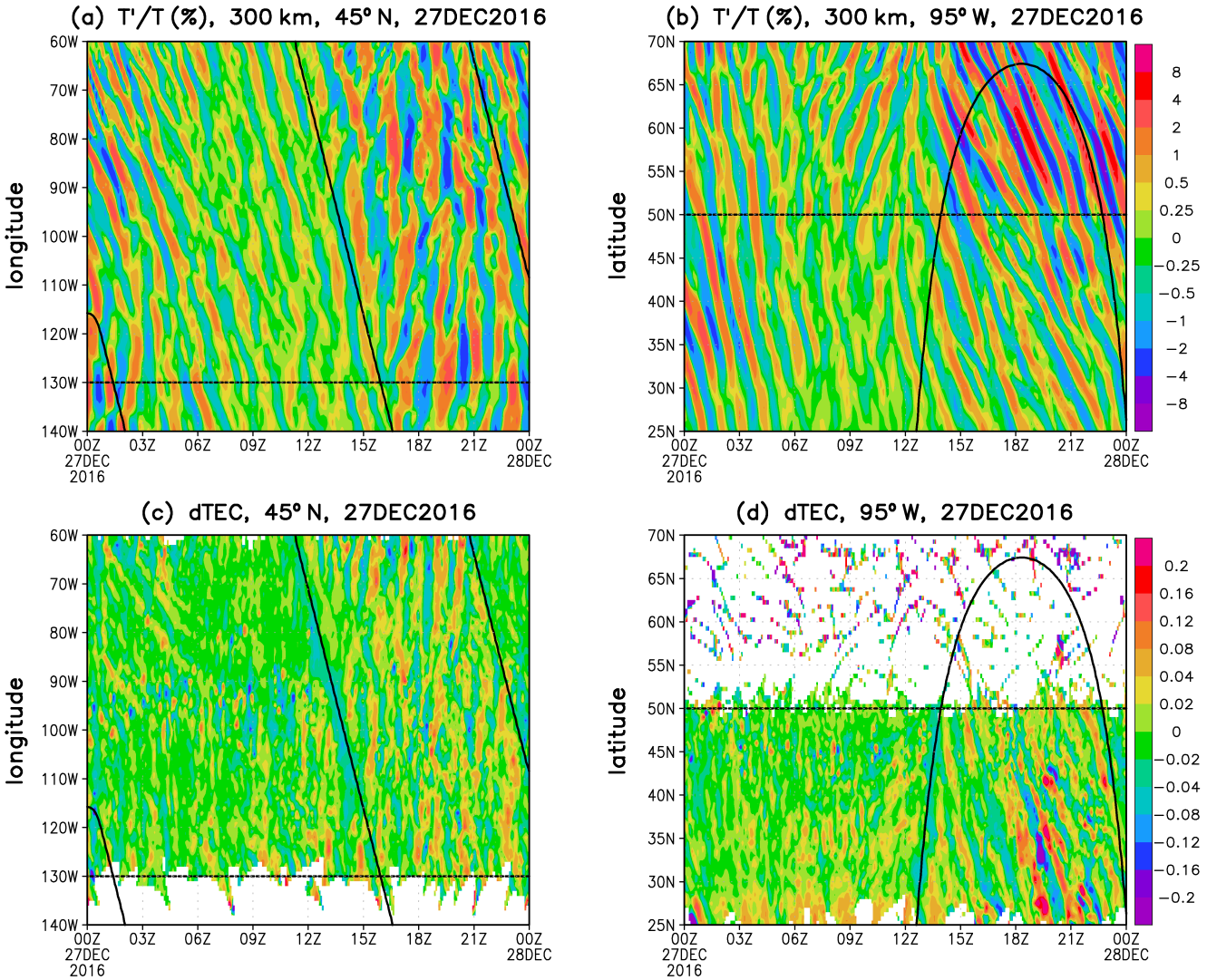

Figure 12. Keograms of simulated gravity waves and observed differential TEC (dTEC) perturbations on 27 December 2016 over North America. Upper row: Relative temperature perturbations at 300 km height at 45°N and from 140 to 60°W (panel (a)), and at 95°W and from 25 to 70°N (panel (b)). Lower row: Same as upper row, but for the dTEC. The horizontal black lines mark 130°W (left columns) and 50°N (right column) to facilitate the comparison of the upper and lower panels. Sunrise and sunset are indicated by slanted (left) and curved (right) black lines.

presumably caused by geomagnetic effects. Apart from this TID, the geographical differences between the two regions regarding the response to the SSW are consistent among the simulated GWs and the dTEC.

When the polar vortex is reestablished in February, we would expect that the GW activity in the thermosphere and the GW-induced TEC perturbations would go back to the conditions before the SSW. However, we have seen from Figures 1 and 2 that only a weak polar vortex follows after the SSW 2017 in February 2017, and that the zonal GW drag in the middle and upper atmosphere during that period is much weaker than during late December 2016 and early January 2017. We therefore expect also weaker GW amplitudes and weaker MSVC, with corresponding consequences for the dTEC. Figures 15 and 16 show keograms analogous to Figures 11 and 12 (or Figures 13 and 14), respectively, on 8 February 2017. We picked this day because a new polar vortex is present and the aforementioned geomagnetic activity period has ceased. The GW propagation (upper panels in Figures 15 and 16) show similar changes during the course of the day to what we have noted for 27 December, namely from eastward in the morning to southward around noon and in the afternoon, and to westward after nightfall. The amplitudes, however, are much weaker than on 27 December 2016, as expected. That is, this difference between early February and late December is most likely a consequence of a weaker polar vortex, giving rise to weaker primary GW effects in the stratosphere and mesosphere, and therefore to weaker amplitudes of higher-order

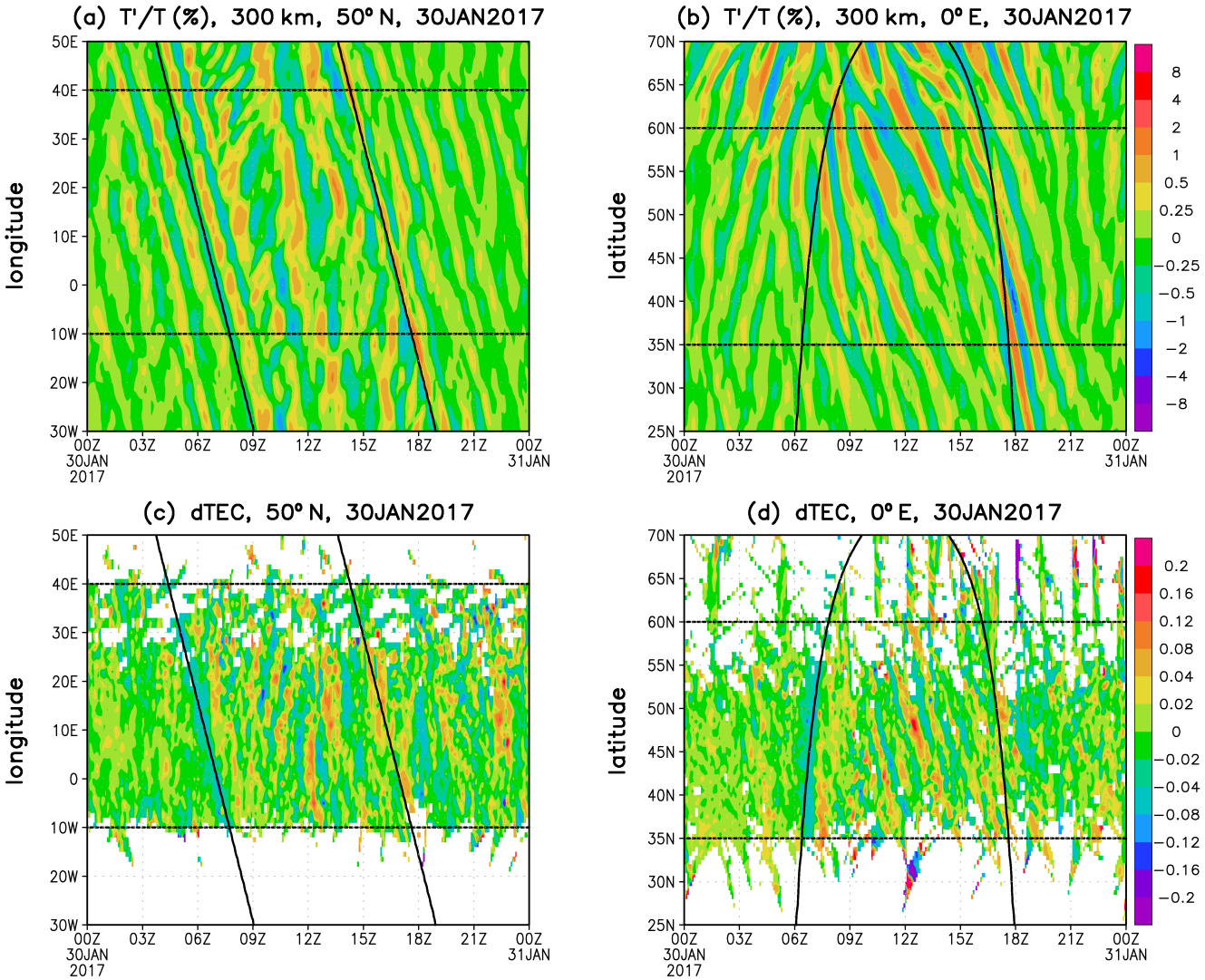

Figure 13. Same as Figure 11, but for 30 January 2017.

GWs in the thermosphere. The dTEC on 8 February 2017 (lower panels in Figures 15 and 16) reflect again the wave characteristics of the simulated GWs. Furthermore, the dTEC amplitudes are weaker than on 27 December 2016, which is consistent with the assumption that these perturbations are largely caused by GWs from below via MSVC.

7. Summary and Concluding Remarks

MSVC is essential to understand the GW activity in the winter middle and upper atmosphere (Becker & Vadas, 2018, 2020; Harvey et al., 2022; Vadas & Becker, 2018, 2019; Vadas et al., 2018, 2019). Since no GW parameterization exists to date that includes MSVC, a GW-resolving whole-atmosphere GCM is required to simulate this coupling. The HIAMCM is such a model. Note that the resolved GWs in high-resolution models are not only limited by the numerical resolution, but also by the methods by which subgrid scales and molecular diffusion are taken into account. This is crucial for the simulated wave-mean flow interactions, and therefore for the simulated MSVC. The HIAMCM employs advanced methods to represent vertical and horizontal diffusion from non-resolved turbulence and from molecular viscosity and heat conduction.

We used the nudged HIAMCM to simulate the Arctic winter season 2016–2017, including the SSW in late January/early February, in order to investigate the response of MSVC to the variability of the polar vortex. For the

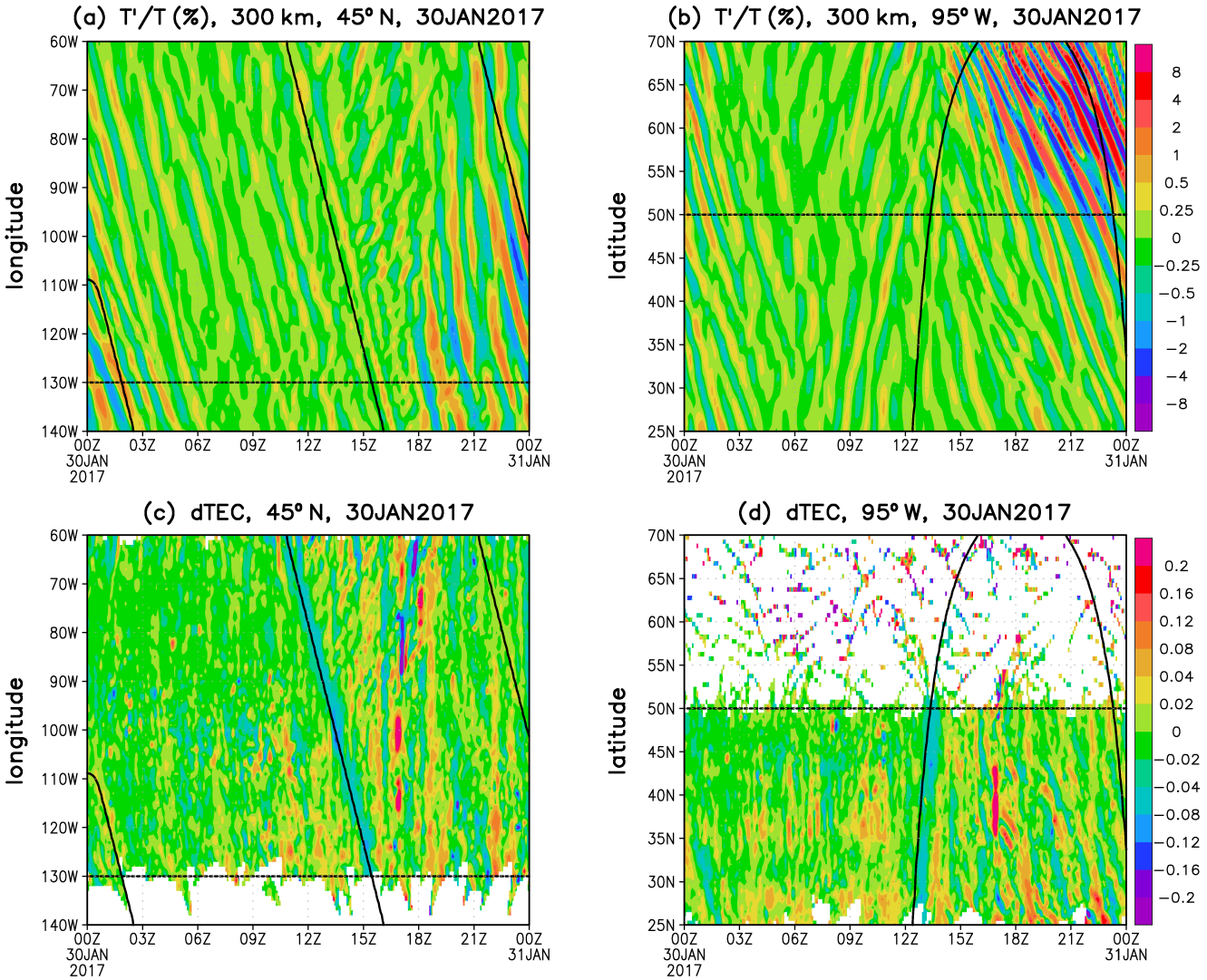

Figure 14. Same as Figure 12, but for 30 January 2017.

period when the polar vortex was strong (late December 2016–early January 2017), our simulation confirms the zonal-mean pattern of the wintertime GW drag noted in earlier studies, namely primary westward GW drag in the mesosphere and secondary/higher-order eastward GW drag in the mesopause region and lower thermosphere. In addition, there is eastward higher-order GW drag in the mid and upper thermosphere at high latitudes. During the SSW, there is primary eastward GW drag in the mesosphere, as is expected from the wind reversal, while higher-order GWs generate only weak effects at higher altitudes. The overall wintertime GW activity from the stratosphere to the thermosphere is found to be much weaker during the SSW and during the weak-vortex period following the SSW than during the strong vortex period.

The weakening of GW activity from the mesopause region on is due to weaker MSVC. This can be explained as follows: First, it is well known that westward propagating primary GWs break at higher altitudes and impart stronger drag when the vortex is stronger and less variable (e.g., Karlsson & Becker, 2016). Second, Vadas and Becker (2019, their Equation 9) showed that the breaking heights of the primary westward propagating GWs strongly affect the secondary GWs. More specifically, assuming similar intermittency and spatial localization of the body forces from primary GWs, the secondary GWs have stronger amplitudes when the momentum deposition from the primary waves occurs at higher altitudes. As a consequence, the higher-order GWs generated from the dissipation of the secondary GWs will have larger amplitudes for a stronger polar vortex. This interpretation is consistent with recent results of Harvey et al. (2022) who argued that the effects from secondary

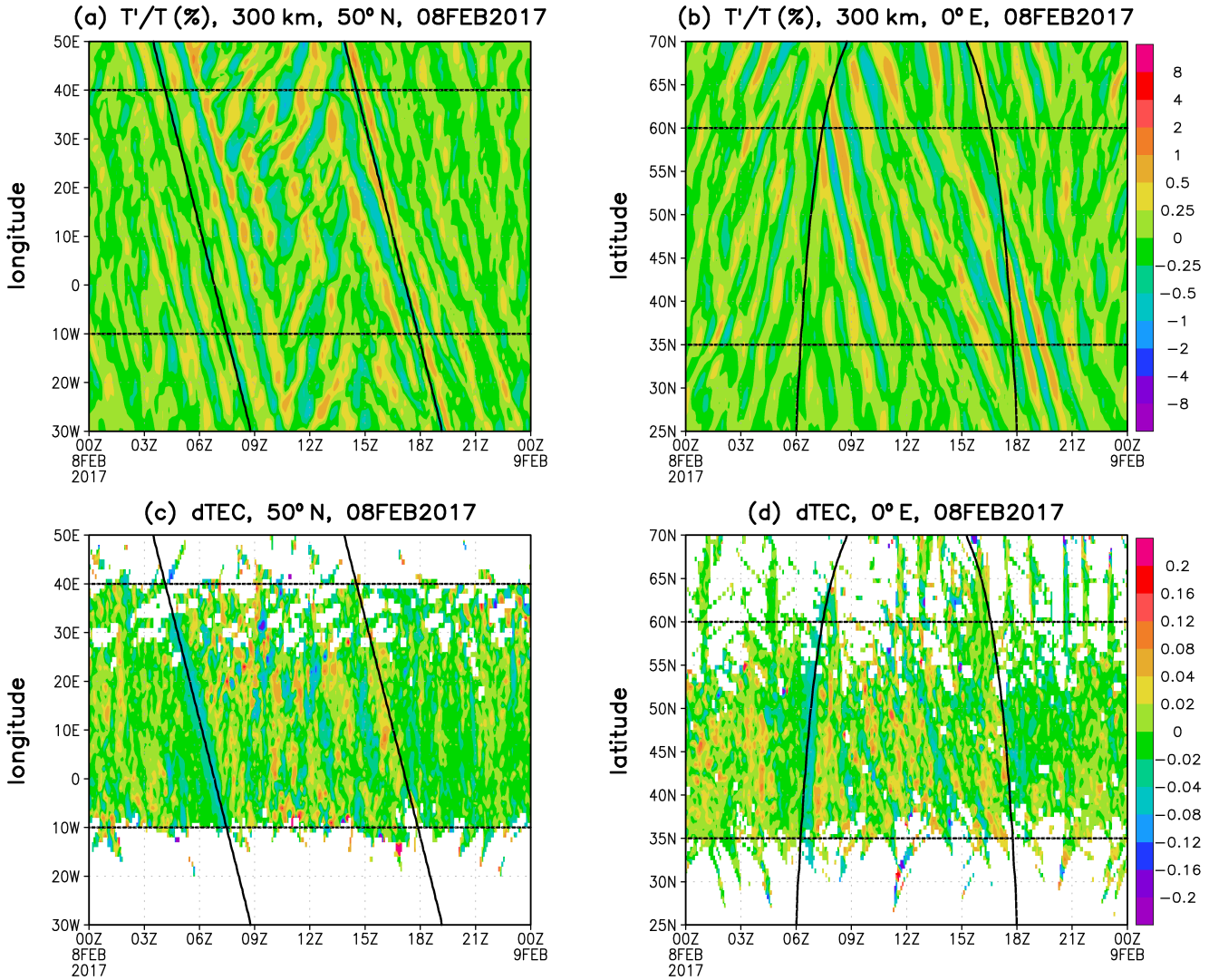

Figure 15. Same as Figure 11, but for 8 February 2017.

GWs (which are neglected in models with GW parameterization) are less significant when the polar vortex is weak and perturbed. It is furthermore consistent with a recent comparison of mean winds in the MLT from radar observations and community models with parameterized GWs by Stober and Kuchar, et al. (2021), who found larger model deficiencies in the southern than northern winter MLT. Also the hemispheric difference in the simulated wintertime secondary GW activity reported by Becker et al. (2020) and Avsarkisov et al. (2022), with stronger secondary GWs in the southern hemisphere, lends further support to the causality that on average, a weaker vortex leads to weaker MSVC. In this context, an SSW can be considered as an extreme event of a weak polar vortex that is even characterized by temporally summer-like conditions with respect to the zonal flow. Even though eastward propagating primary GWs can propagate into the upper mesosphere during an SSW before they dissipate, they typically have much lower amplitudes than the corresponding westward propagating GWs during a strong vortex. Therefore, an SSW is characterized by reduced MSVC similarly to a strongly weakened and perturbed polar vortex.

A potentially important mechanism for the in situ generation of GWs in the winter stratosphere is spontaneous emission (e.g., Sato & Yoshiki, 2008; Zhang, 2004). Since this mechanism strongly depends on vertical wind shear beneath the wind maximum of the polar vortex (Becker et al., 2022), we argue that the response of spontaneous emission likely contributes to reduced MSVC during a weak-vortex period or an SSW event. Yasui

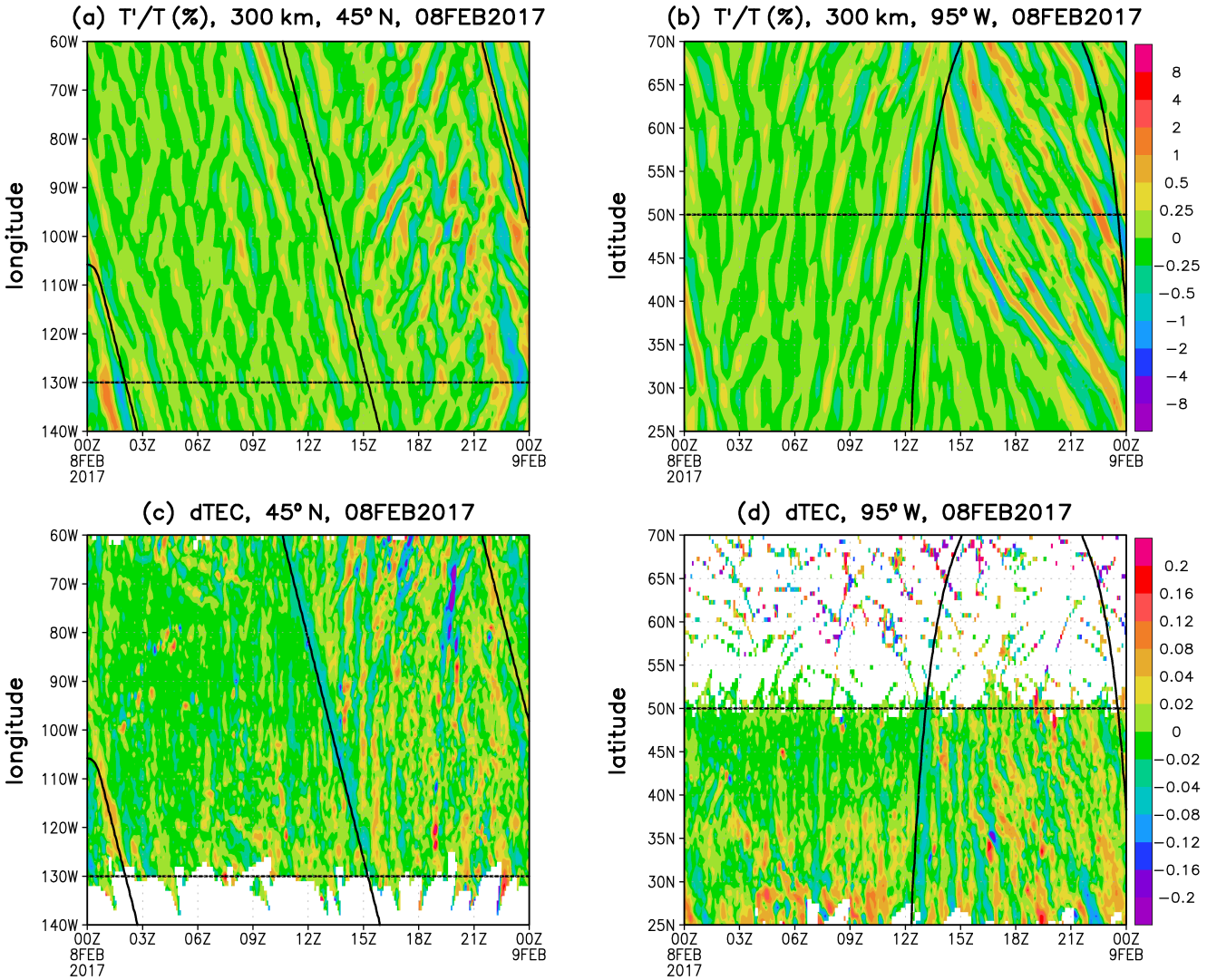

Figure 16. Same as Figure 12, but for 8 February 2017.

et al. (2018) found that the GW generation in the MLT of a GCM is correlated with low Richardson numbers. In this context we note that the dissipation of GWs that have propagated from below and dissipate in the MLT is associated with low Richardson number as well (Becker, 2009). We checked but did not show in this paper that the average Richardson number criterion that is part of the diffusion scheme of the HIAMMCM (see Becker & Vadas, 2020, Equations A6–A8) is about three times stronger in the winter MLT during the strong vortex period than during the SSW period. Hence, reduced MSVC implies larger Richardson numbers in the MLT. Therefore, even if the mechanism proposed by Yasui et al. (2018) was distinct from MSVC, it would add to reduced GW activity in the thermosphere during an SSW.

Our study confirms former model results that the wintertime higher-order GWs show partial concentric ring structures above their sources in the lower thermosphere (e.g., Vadas & Becker, 2019). Only those higher-order GWs can propagate to higher altitudes for which the propagation direction projected on the mean wind associated with the in situ generated diurnal tide is against this wind. This is a consequence of the tidal-induced directional dissipation of GWs, as argued by Fritts and Vadas (2008). We found that the tidal winds in the mid and upper thermosphere at middle to high latitudes are strongest during the daytime and have a predominant poleward direction. As a result, the simulated GWs have the largest amplitudes around local time noon and

early afternoon and they propagate predominantly equatorward during this time. These GWs propagate mainly eastward during the morning and westward after nightfall. We presented a 10-day-average of the daily cycle of the GW activity in the winter thermosphere for the strong vortex period and during the SSW (Figures 9 and 10), which show that the GW activity is, on average, subject to a pronounced GW maximum during noon and afternoon at middle to high latitudes, and that the strongest momentum flux component associated with this maximum is equatorward.

In this study, the HIAMCM is extended by a simple parameterization of the ion drag over the polar cap that forces the auroral circulation. This forcing adds an additional, horizontally rotational component to the cross-polar tidal flow (e.g., Forbes, 2007). Since this flow is slightly shifted into the dawn sector, it causes westward flow in the zonal mean at polar latitudes (e.g., Drob et al., 2015). Due to this westward flow during dawn at polar latitudes, the aforementioned daytime GW maximum extends into the dawn sector at polar latitudes. The GWs in this region propagate mainly eastward, and their dissipation causes the aforementioned eastward GW drag in the wintertime middle and upper thermosphere at high latitudes in the zonal mean. The auroral circulation also has an effect on the EPF divergence of the tides. Since the tidal flow is strongly forced over the polar caps by the additional ion drag, the EPF divergence is eastward in this region, while the dissipation of the tides at higher altitudes or farther away from the poles gives rise to westward EPF divergence, as expected.

The main result from this paper is a strong reduction of thermospheric GWs that results from reduced MSVC during the SSW in January 2017, and also during the weak vortex period thereafter. To validate this model results, we compared keograms of the simulated GWs at 300 km height over Europe and North America to perturbations in the observed GNSS TEC during selected days of low geomagnetic activity. We found very good agreement for the wave characteristics (evolution of the propagation direction during the course of the day, typical wavelengths and periods), lending support to the notion that the quiet-time TEC perturbations (dTEC) are driven by GWs from below. In accordance with the model results, we furthermore found a clear reduction in the dTEC during the SSW as compared to late December. This reduction was still visible in both the simulated GWs and the dTEC shortly after the SSW when a weak polar vortex was reestablished in early February. All these new results are consistent with former observational results about a positive correlation between the daytime amplitudes of TIDs and the strength of the polar vortex (e.g., Frissell et al., 2016; Nayak & Yiğit, 2019). Finally, both the simulated GWs and observed TID perturbations showed that the weakening effect in late January and early February 2017 was more efficient over Europe than over North America. Such regional differences may be different for different SSW events.

The agreement between the simulated GWs in the thermosphere and dTEC, as well as their responses to an SSW followed by a weak vortex period, suggests that wintertime MSVC is simulated by the HIAMCM with a very good degree of realism. More specifically, given the limited spatial resolution of the HIAMCM, the macro-turbulent diffusion scheme is tuned in a way that the resolved primary and higher-order GWs dissipate at the proper times and locations (higher-order GWs dissipate directly from molecular viscosity in the HIAMCM only above about 200 km). On the other hand, wintertime primary GWs are often small-scale orographic waves (Kruse et al., 2022); these waves are not resolved by the HIAMCM. The question remains to what extent wintertime small-scale primary GWs contribute to MSVC and the resulting higher-order GWs in the thermosphere. This question can be addressed in the future when comparisons with simulations performed at higher resolutions become feasible.

Appendix A: Ion Drag Parameterization for the Auroral Circulaton

In the following we describe a simple parameterization of the ion drag in the polar region that forces the neutral flow in the thermosphere from the dayside to the nightside, also known as the auroral circulation (Forbes, 2007). This dynamical feature was previously not included in the HIAMCM. The ion drag over the polar cap is induced by the fact that part of the interstellar magnetic field associated with the solar wind connects with the geomagnetic field. This causes an electric field that points into the dawn-to-dusk direction and leads to an $E \times B$ drift in the polar ionosphere from the dayside to the nightside, which in turn forces corresponding neutral winds across the poles by neutral-ion collisions. Unlike the thermally forced tidal winds that are also across the pole from the dayside to the nightside, the auroral circulation can be described

to very good approximation by a horizontal streamfunction, that is, by a purely rotational flow in the horizontal plane.

To formulate a simple parameterization of the additional ion drag at polar latitudes, we define a horizontal streamfunction that corresponds to the auroral circulation as

$$\psi_{ac}(\lambda, \phi, p, t) = (\psi_1(\lambda, \phi, t) + \psi_2(\lambda, \phi, t)) \times \zeta(p). \tag{A1}$$

Here, ψ_1 and ψ_2 specify the horizontal streamfunction contributions from the dawn and dusk sectors, respectively, and ζ is a vertical profile. As usual, λ and ϕ are longitude and latitude, p is pressure, and t is time. We define

$$\psi_i(\lambda, \phi, t) = \psi_{i0} \begin{cases} \cos\left(\frac{1}{2}\,\pi\, r_i(\lambda, \phi, t)/d_i\right)^2, & r_i/d_i < 1 \\ 0, & \text{else} \end{cases} \tag{A2}$$

$$r_i(\lambda, \phi, t) = \sqrt{(x(\lambda, \phi) - x_i(t))^2 + (y(\lambda, \phi) - y_i(t))^2} \tag{A3}$$

$$x(\lambda, \phi) = a_e\,(1 - 2\phi/\pi)\,\cos\,\lambda \tag{A4}$$

$$y(\lambda, \phi) = a_e\,(1 - 2\phi/\pi)\,\sin\,\lambda \tag{A5}$$

$$x_i(t) = a_e\,(1 - 2\phi_i/\pi)\,\cos\,(\lambda_i - 2\pi\, t/(1\,\text{day})) \tag{A6}$$

$$y_i(t) = a_e\,(1 - 2\phi_i/\pi)\,\sin\,(\lambda_i - 2\pi\, t/(1\,\text{day}))\,, \tag{A7}$$

where $i = 1, 2$ and a_e denotes the earth radius. The free parameters are specified as $(\psi_{10}, \psi_{20}) = a_e \times (-48,$ 64 m s^{-1}), $(\lambda_1, \lambda_2) = (76°, 270°)$E, $(\phi_1, \phi_2) = (64°, 76°)$N, $(d_1, d_2) = (2, 3) \times 10^6$ m. An analogous formulation is used for the southern hemisphere.

Using $h = \ln(p_{00}/p)$ with $p_{00} = 1{,}013$ hPa, we write the vertical profile as

$$\zeta(p) = \begin{cases} 0, & h(p) \geq h_4 \\ \cos\left(\frac{1}{2}\,\pi\,(h(p) - h_3)/(h_4 - h_3)\right), & h_4 > h(p) > h_3 \\ 1, & h_3 \geq h(p) \geq h_2 \\ \cos\left(\frac{1}{2}\,\pi\,(h(p) - h_2)/(h_2 - h_1)\right), & h_2 > h(p) > h_1 \\ 0, & h_1 \geq h(p) \end{cases} \tag{A8}$$

Here, $h_i = \ln(p_{00}/p_i)$ and the corresponding pressure levels were set to $p_1 = 2 \times 10^{-5}$, $p_2 = 2 \times 10^{-7}$, $p_3 = 1 \times 10^{-8}$, and $p_4 = 2 \times 10^{-11}$ hPa.

Figure A1 shows the horizontal streamfunction (colors) used for forcing of the auroral circulation in the NH at 00:00, 06:00, 12:00, and 18:00 UT. The pressure level is 10^{-7} hPa ($\zeta = 1$). To indicate the wind speeds associated with ψ_{ac}, the figure includes the 15 and 25 m s^{-1} horizontal wind speed contours. In the HIAMCM we use this streamfunction to add a corresponding forcing to right-hand side of the model's relative vorticity equation:

$$\partial_t \xi \rightarrow \partial_t \xi + \tau^{-1} \nabla^2 \psi_{ac}. \tag{A9}$$

Here, the time constant is $\tau = 900$ s and ∇ is the horizontal gradient operator in spherical geometry.

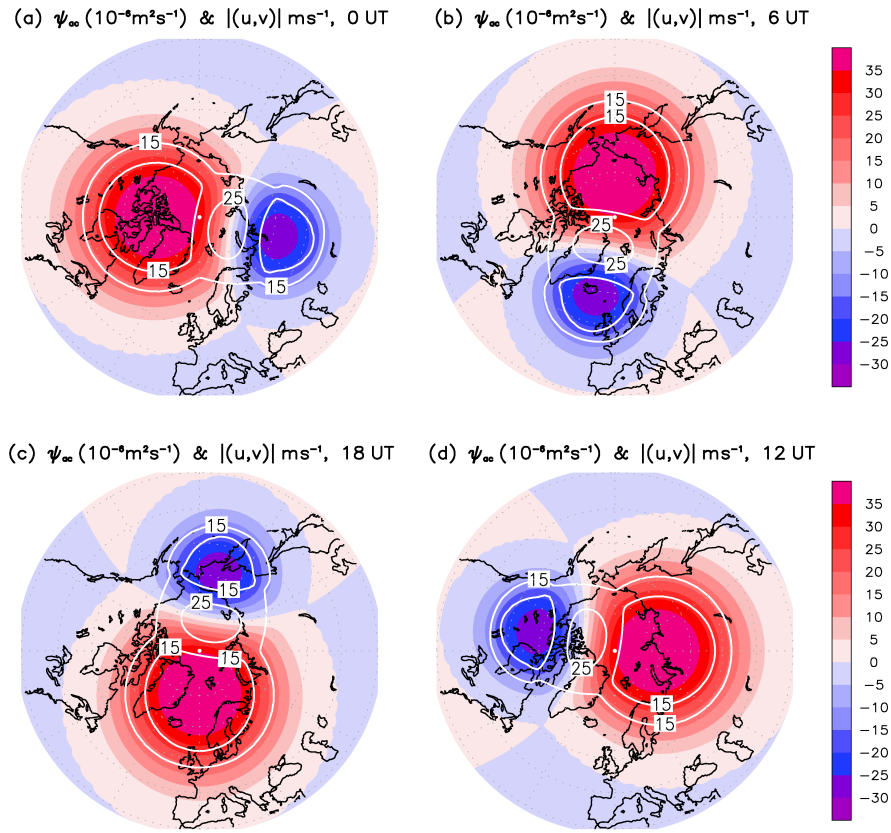

Figure A1. Horizontal mass streamfunction (colors, unit 10^6 m^2 s^{-1}) used to force the auroral circulation in the northern thermosphere at (a) 00:00, (b) 06:00, (c) 18:00, and (d) 12:00 UT. The white contours mark the 15 and 25 m s^{-1} horizontal wind speeds. The circulation is clockwise about the maximum and counterclockwise about the minimum of the streamfunction.

Data Availability Statement

The MERRA-2 reanalysis data used in this study are publicly available at https://disc.gsfc.nasa.gov/dataset. GPS TEC data products and access through the CEDAR Madrigal distributed data system (http://cedar.openmadrigal.org/) are provided to the community by the MIT Haystack Observatory. All data shown in this paper are available via NWRA's website under https://www.cora.nwra.com/~erich.becker/Becker-etal-JGRSP-2022-files.

Acknowledgments
Model simulations were performed by the authors. Model documentations can be found in Section 2, in the Appendix, as well as in Becker and Vadas (2020) and Becker et al. (2022). EB, LPG, and VLH were supported by NASA Grant 80NSSC19K0834. EB, VLH, and SLV acknowledge support by NASA Grant 80NSSC20K0628. SLV and EB were furthermore supported by NSF Grant AGS-1832988 and NASA Grant 80NSSC19K0836. LPG acknowledges further support by ONR Grant N00014-17-1-2186. TEC data processing at MIT Haystack Observatory was supported by NSF Grant AGS-1952737. We thank the Leibniz Institute of Atmospheric Physics at the University of Rostock and the NASA HEC for providing the HPC facilities used in this study. The comments of two anonymous reviewers are gratefully acknowledged.

References

Andrews, D. G., Holton, J. R., & Leovy, C. B. (1987). *Middle Atmosphere Dynamics, International Geophysics Series* (Vol. 40). Academic Press.
Avsarkisov, V., Becker, E., & Renkwitz, T. (2022). Turbulent coherent structures in the middle atmosphere: Theoretical estimates deduced from a gravity-wave resolving general circulation model. *Journal of the Atmospheric Sciences*, *79*(4), 933–952. https://doi.org/10.1175/JAS-D-21-0005.1
Baldwin, M. P., Ayarzagüena, B., Birner, T., Butchart, N., Butler, A. H., Charlton-Perez, A. J., et al. (2021). Sudden stratospheric warmings. *Reviews of Geophysics*, *59*(1), e2020RG000708. https://doi.org/10.1029/2020RG000708
Becker, E. (2009). Sensitivity of the upper mesosphere to the Lorenz energy cycle of the troposphere. *Journal of the Atmospheric Sciences*, *66*(3), 648–666. https://doi.org/10.1175/2008JAS2735.1
Becker, E. (2012). Dynamical control of the middle atmosphere. *Space Science Reviews*, *168*(1–4), 283–314. https://doi.org/10.1007/s11214-011-9841-5
Becker, E. (2017). Mean-flow effects of thermal tides in the mesosphere and lower thermosphere. *Journal of the Atmospheric Sciences*, *74*(6), 2043–2063. https://doi.org/10.1175/JAS-D-16-0194.1
Becker, E., Grygalashvyly, M., & Sonnemann, G. R. (2020). Gravity wave mixing effects on the OH*-layer. *Advances in Space Research*, *65*(1), 175–188. https://doi.org/10.1016/j.asr.2019.09.043
Becker, E., & Vadas, S. L. (2018). Secondary gravity waves in the winter mesosphere: Results from a high-resolution global circulation model. *Journal of Geophysical Research: Atmospheres*, *123*(5), 2605–2627. https://doi.org/10.1002/2017JD027460
Becker, E., & Vadas, S. L. (2020). Explicit global simulation of gravity waves in the thermosphere. *Journal of Geophysical Research: Space Physics*, *125*(10), e2020JA028034. https://doi.org/10.1029/2020JA028034

Becker, E., Vadas, S. L., Bossert, K., Harvey, V. L., Zülicke, C., & Hoffmann, L. (2022). A high-resolution whole-atmosphere model with resolved gravity waves and specified large-scale dynamics in the troposphere and stratosphere. *Journal of Geophysical Research: Atmospheres*, *127*(2), e2021JD035018. https://doi.org/10.1029/2021JD035018

Bölöni, G., Kim, Y.-H., Borchert, S., & Achatz, U. (2021). Toward transient subgrid-scale gravity wave representation in atmospheric models. Part I: Propagation model including nondissipative wave-mean-flow interactions. *Journal of the Atmospheric Sciences*, *78*(4), 1317–1338. https://doi.org/10.1175/JAS-D-20-0065.1

Bruinsma, S. L., & Forbes, J. M. (2008). Medium- to large-scale density variability as observed by CHAMP. *Space Weather*, *6*(8), S08002. https://doi.org/10.1029/2008SW000411

Butler, A. H., Sjoberg, J. P., Seidel, D. J., & Rosenlof, K. H. (2017). A sudden stratospheric warming compendium. *Earth System Science Data*, *9*(1), 63–76. https://doi.org/10.5194/essd-9-63-2017

Chandran, A., Collins, R. L., Garcia, R. R., Marsh, D. R., Harvey, V. L., Yue, J., & de la Torre, L. (2013). A climatology of elevated stratopause events in the whole atmosphere community climate model. *Journal of Geophysical Research: Atmospheres*, *118*(3), 1234–1246. https://doi.org/10.1002/jgrd.50123

Cho, Y.-M., Shepherd, G. G., Won, Y.-I., Sargoytchev, S., Brown, S., & Solheim, B. (2004). MLT cooling during stratospheric warming events. *Geophysical Research Letters*, *31*(10), L10104. https://doi.org/10.1029/2004GL019552

Conde, M. G., & Nicolls, M. J. (2010). Thermospheric temperatures above Poker Flat, Alaska, during the stratospheric warming event of January and February 2009. *Journal of Geophysical Research*, *115*, D00N05. https://doi.org/10.1029/2010JD014280

Coster, A. J., Goncharenko, L., Zhang, S.-R., Erickson, P. J., Rideout, W., & Vierinen, J. (2017). GNSS observations of ionospheric variations during the 21 August 2017 solar eclipse. *Geophysical Research Letters*, *44*(24), 12041–12048. https://doi.org/10.1002/2017GL075774

Crowley, G., & Rodrigues, F. S. (2012). Characteristics of traveling ionospheric disturbances observed by the TIDDBIT sounder. *Radio Science*, *47*(4), 1–12. https://doi.org/10.1029/2011RS004959

de Wit, R. J., Janches, D., Fritts, D. C., Stockwell, R., & Coy, L. (2017). Unexpected climatological behavior of MLT gravity wave momentum flux in the lee of the Southern Andes hotspot. *Geophysical Research Letters*, *44*(2), 1182–1191. https://doi.org/10.1002/2016GL072311

Drob, D. P., Emmert, J. T., Meriwether, J. W., Makela, J. J., Doornbos, E., Conde, M., et al. (2015). An update to the Horizontal Wind Model (HWM): The quiet time thermosphere. *Earth and Space Science*, *2*(7), 301–319. https://doi.org/10.1002/2014EA000089

Dunkerton, T. J., & Butchart, N. (1984). Propagation and selective transmission of internal gravity waves in a sudden warming. *Journal of the Atmospheric Sciences*, *41*(8), 1143–1460. https://doi.org/10.1175/1520-0469(1984)041<1443:pastoi>2.0.co;2

Dunkerton, T. J., Hsu, F., & McIntyre, M. E. (1981). Some Eulerian and Lagrangian diagnostics for a model stratospheric warming. *Journal of the Atmospheric Sciences*, *38*(4), 819–844. https://doi.org/10.1175/1520-0469(1981)038<0819:SEALDF>2.0.CO;2

Edmon, H. J., Jr., Hoskins, B. J., & McIntyre, M. E. (1980). Eliassen-Palm cross sections for the troposphere. *Journal of the Atmospheric Sciences*, *37*(12), 2600–2616. https://doi.org/10.1175/1520-0469(1980)037<2600:epcsft>2.0.co;2

England, S. L., Greer, K. R., Zhang, S.-R., Evans, S., Solomon, S. C., Eastes, R. W., et al. (2021). First comparison of traveling atmospheric disturbances observed in the middle thermosphere by Global-scale Observations of the Limb and Disk to traveling ionospheric disturbances seen in ground-based total electron content observations. *Journal of Geophysical Research: Space Physics*, *126*(6), e2021JA029248. https://doi.org/10.1029/2021JA029248

Forbes, J. M. (2007). Dynamics of the thermosphere. *Journal of the Meteorological Society of Japan. Ser. II*, *85B*, 193–213. https://doi.org/10.2151/jmsj.85b.193

Frissell, N. A., Baker, J. B. H., Ruohoniemi, J. M., Greenwald, R. A., Gerrard, A. J., Miller, E. S., & West, M. L. (2016). Sources and characteristics of medium-scale traveling ionospheric disturbances observed by high-frequency radars in the north American sector. *Journal of Geophysical Research: Space Physics*, *121*(4), 3722–3739. https://doi.org/10.1002/2015JA022168

Fritts, D. C., Dong, W., Lund, T. S., Wieland, S., & Laughman, B. (2020). Self-acceleration and instability of gravity wave packets: 3. Three-dimensional packet propagation, secondary gravity waves, momentum transport, and transient mean forcing in tidal winds. *Journal of Geophysical Research: Atmospheres*, *125*, e2019JD030692. https://doi.org/10.1029/2019JD030692

Fritts, D. C., & Vadas, S. L. (2008). Gravity wave penetration into the thermosphere: Sensitivity to solar cycle variations and mean winds. *Annales Geophysicae*, *26*(12), 3841–3861. https://doi.org/10.5194/angeo-26-3841-2008

Fuller-Rowell, T., Akmaev, R., Wu, F., Fedrizzi, M., Viereck, R. A., & Wang, H. (2011). Did the January 2009 sudden stratospheric warming cool or warm the thermosphere? *Geophysical Research Letters*, *38*(18), L18104. https://doi.org/10.1029/2011GL048985

Fuller-Rowell, T., Wu, F., Akmaev, R., Fang, T.-W., & Araujo-Pradere, E. (2010). A whole atmosphere model simulation of the impact of a sudden stratospheric warming on thermosphere dynamics and electrodynamics. *Journal of Geophysical Research*, *115*(A10), A00G08. https://doi.org/10.1029/2010JA015524

Funke, B., Ball, W., Bender, S., Gardini, A., Harvey, V. L., Lambert, A., et al. (2017). HEPPA-II model-measurement intercomparison project: EPP indirect effects during the dynamically perturbed NH winter 2008–2009. *Atmospheric Chemistry and Physics*, *17*(5), 3573–3604. https://doi.org/10.5194/acp-17-3573-2017

Funke, B., López-Puertas, M., Bermejo-Pantaleón, D., Garcia-Comas, M., Stiller, G. P., von Clarmann, T., et al. (2010). Evidence for dynamical coupling from the lower atmosphere to the thermosphere during a major stratospheric warming. *Geophysical Research Letters*, *37*(13), L138061–L138065. https://doi.org/10.1029/2010GL043619

Garcia, R. F., Bruinsma, S. L., Massarweh, L., & Doornbos, E. (2016). Medium-scale gravity wave activity in the thermosphere inferred from GOCE data. *Journal of Geophysical Research: Space Physics*, *121*(8), 8089–8102. https://doi.org/10.1002/2016JA022797

Goncharenko, L. P., Chau, J. L., Liu, H.-L., & Coster, A. J. (2010). Unexpected connections between the stratosphere and ionosphere. *Geophysical Research Letters*, *37*(10), L10101. https://doi.org/10.1029/2010GL043125

Goncharenko, L. P., Harvey, V. L., Liu, H., & Pedatella, N. M. (2021). Sudden stratospheric warming impacts on the ionosphere-thermosphere system – A review of recent progress. In C. Huang, G. Lu, Y. Zhang, & L. J. Paxton (Eds.), *Advances in ionospheric research: Current understanding and challenges*. American Geophysical Union. https://doi.org/10.1002/9781119815617.ch16

Goncharenko, L. P., & Zhang, S.-R. (2008). Ionospheric signatures of sudden stratospheric warming: Ion temperature at middle latitude. *Geophysical Research Letters*, *35*(21), L21103. https://doi.org/10.1029/2008GL035684

Harvey, V. L., Pedatella, N., Becker, E., & Randall, C. E. (2022). Evaluation of polar winter mesopause wind in WACCMX+DART. *Journal of Geophysical Research: Atmospheres*, *127*(15), e2022JD037063. https://doi.org/10.1029/2022JD037063

Harvey, V. L., Randall, C. E., Becker, E., Smith, A. K., Barden, C. G., France, J. A., & Goncharenko, L. P. (2019). Evaluation of the mesospheric polar vortices in WACCM. *Journal of Geophysical Research: Atmospheres*, *124*(20), 10626–10645. https://doi.org/10.1029/2019JD030727

Heale, C. J., Bossert, K., & Vadas, S. L. (2022). 3D numerical simulation of secondary wave generation from mountain wave breaking over Europe. *Journal of Geophysical Research: Atmospheres*, *127*(5), e2021JD035413. https://doi.org/10.1029/2021JD035413

Hindley, N. P., Mitchell, N. J., Cobbett, N., Smith, A. K., Fritts, D. C., Janches, D., et al. (2022). Radar observations of winds, waves and tides in the mesosphere and lower thermosphere over South Georgia Island (54°S, 36°W) and comparison to WACCM simulations. *Atmospheric Chemistry and Physics*, *22*(14), 9435–9459. https://doi.org/10.5194/acp-2021-981

Hoffmann, P., Becker, E., Singer, W., & Placke, M. (2010). Seasonal variation of mesospheric waves at northern middle and high latitudes. *Journal of Atmospheric and Solar-Terrestrial Physics*, *72*(14–15), 1068–1079. https://doi.org/10.1016/j.jastp.2010.07.002

Holton, J. R. (1983). The influence of gravity wave breaking on the general circulation of the middle atmosphere. *Journal of the Atmospheric Sciences*, *40*(10), 2497–2507. https://doi.org/10.1175/1520-0469(1983)040<2497:tiogwb>2.0.co;2

Hong, S.-S., & Lindzen, R. S. (1976). Solar semidiurnal tide in the thermosphere. *Journal of the Atmospheric Sciences*, *33*(1), 135–153. https://doi.org/10.1175/1520-0469(1976)033<0135:sstitt>2.0.co;2

Jonah, O. F., Coster, A. J., Zhang, S.-R., Goncharenko, L. P., Erickson, P. J., de Paula, E. R., & Kherani, E. A. E. R. (2018). TID observations and source analysis during the 2017 Memorial Day weekend geomagnetic storm over North America. *Journal of Geophysical Research: Space Physics*, *123*(10), 8749–8765. https://doi.org/10.1029/2018JA025367

Karlsson, B., & Becker, E. (2016). How does interhemispheric coupling contribute to cool down the summer polar mesosphere? *Journal of Climate*, *29*(24), 8807–8821. https://doi.org/10.1175/JCLI-D-16-0231.1

Karlsson, B., McLandress, C., & Shepherd, T. G. (2009). Inter-hemispheric mesospheric coupling in a comprehensive middle atmosphere model. *Journal of Atmospheric and Solar-Terrestrial Physics*, *71*(3–4), 518–530. https://doi.org/10.1016/j.jastp.2008.08.006

Kruse, C. G., Alexander, M. J., Hoffmann, L., van Niekerk, A., Polichtchouk, I., Bacmeister, J. T., et al. (2022). Observed and modeled mountain waves from the surface to the mesosphere near the Drake Passage. *Journal of the Atmospheric Sciences*, *79*(4), 909–932. https://doi.org/10.1175/JAS-D-21-0252.1

Kurihara, J., Ogawa, Y., Oyama, S., Nozawa, S., Tsutsumi, M., Hall, C. M., et al. (2010). Links between a stratospheric sudden warming and thermal structures and dynamics in the high-latitude mesosphere, lower thermosphere, and ionosphere. *Geophysical Research Letters*, *37*(13), L13806. https://doi.org/10.1029/2010GL043643

Labitzke, K. (1972). The interaction between stratosphere and mesosphere in winter. *Journal of the Atmospheric Sciences*, *29*(7), 1395–1399. https://doi.org/10.1175/1520-0469(1972)029<1395:tibsam>2.0.co;2

Limpasuvan, V., Richter, J. H., Orsolini, Y. J., Stordal, F., & Kvissel, O.-K. (2012). The roles of planetary and gravity waves during a major stratospheric sudden warming as characterized in WACCM. *Journal of Atmospheric and Solar-Terrestrial Physics*, *78–79*, 84–98. https://doi.org/10.1016/j.jastp.2011.03.004

Liu, H.-L., McInerney, J. M., Santos, S., Lauritzen, P. H., Taylor, M. A., & Pedatella, N. M. (2014). Gravity waves simulated by high-resolution whole atmosphere community climate model. *Geophysical Research Letters*, *41*(24), 9106–9112. https://doi.org/10.1002/2014GL062468

Liu, H.-L., & Roble, R. G. (2002). A study of a self-generated stratospheric sudden warming and its mesospheric-lower thermospheric impacts using the coupled TIME-GCM/CCM3. *Journal of Geophysical Research*, *107*(D23), ACL 15-1–ACL 15-18. https://doi.org/10.1029/2001JD001533

Manney, G. L., Krüger, K., Pawson, S., Minschwaner, K., Schwartz, M. J., Daffer, W. H., et al. (2008). The evolution of the stratopause during the 2006 major warming: Satellite data and assimilated meteorological analyses. *Journal of Geophysical Research*, *113*(D11), D11115. https://doi.org/10.1029/2007JD009097

Manney, G. L., Schwartz, M. J., Krüger, K., Santee, M. L., Pawson, S., Lee, J. N., et al. (2009). Aura Microwave Limb Sounder observations of dynamics and transport during the record-breaking 2009 Arctic stratospheric major warming. *Geophysical Research Letters*, *36*(12), L12815. https://doi.org/10.1029/2009GL038586

Matsuno, T. (1971). A dynamical model of the stratospheric sudden warming. *Journal of the Atmospheric Sciences*, *28*(8), 1479–1494. https://doi.org/10.1175/1520-0469(1971)028<1479:admots>2.0.co;2

McIntyre, M. (1982). How well do we understand the dynamics of stratospheric warmings? *Journal of the Meteorological Society of Japan. Ser. II*, *60*(1), 37–65. https://doi.org/10.2151/jmsj1965.60.1_37

McLandress, C., Scinocca, J. F., Shepherd, T. G., Reader, M. C., & Manney, G. L. (2013). Dynamical control of the mesosphere by orographic and nonorographic gravity wave drag during the extended northern winters of 2006 and 2009. *Journal of the Atmospheric Sciences*, *70*(7), 2152–2169. https://doi.org/10.1175/JAS-D-12-0297.1

McLandress, C., Ward, W. E., Fomichev, V. I., Semeniuk, K., Beagley, S. R., McFarlane, N. A., & Shepherd, T. G. (2006). Large-scale dynamics of the mesosphere and lower thermosphere: An analysis using the extended Canadian Middle Atmosphere Model. *Journal of Geophysical Research*, *111*(D17), D17111. https://doi.org/10.1029/2005JD006776

Nayak, C., & Yiğit, E. (2019). Variation of small-scale gravity wave activity in the ionosphere during the major sudden stratospheric warming event of 2009. *Journal of Geophysical Research: Space Physics*, *124*(1), 470–488. https://doi.org/10.1029/2018JA026048

Negrea, C., Zabotin, N., Bullett, T., Fuller-Rowell, T., Fang, T.-W., & Codrescu, M. (2016). Characteristics of acoustic gravity waves obtained from Dynasonde data. *Journal of Geophysical Research: Space Physics*, *121*(4), 3665–3680. https://doi.org/10.1002/2016JA022495

Nicolls, M. J., Vadas, S. L., Aponte, N., & Sulzer, M. P. (2014). Horizontal wave parameters of daytime thermospheric gravity waves and E region neutral winds over Puerto Rico. *Journal of Geophysical Research: Space Physics*, *119*(1), 575–600. https://doi.org/10.1002/2013JA018988

Ortland, D. A., & Alexander, M. J. (2006). Gravity wave influence on the global structure of the diurnal tide in the mesosphere and lower thermosphere. *Journal of Geophysical Research*, *111*(A10), A10S10. https://doi.org/10.1029/2005JA011467

Park, J., Lühr, H., Lee, C., Kim, Y. H., Jee, G., & Kim, J.-H. (2014). A climatology of medium-scale gravity wave activity in the midlatitude/low-latitude daytime upper thermosphere as observed by CHAMP. *Journal of Geophysical Research: Space Physics*, *19*(3), 2187–2196. https://doi.org/10.1002/2013JA019705

Pitteway, M. L. V., & Hines, C. O. (1963). The viscous damping of atmospheric gravity waves. *Canadian Journal of Physics*, *41*(12), 1935–1948. https://doi.org/10.1139/p63-194

Randall, C. E., Harvey, V. L., Siskind, D. E., France, J., Bernath, P. F., Boone, C. D., & Walker, K. A. (2009). NO_x decent in the Arctic middle atmosphere in early 2009. *Geophysical Research Letters*, *36*(18), L18811. https://doi.org/10.1029/2009GL039706

Sato, K., & Yoshiki, M. (2008). Gravity wave generation around the polar vortex in the stratosphere revealed by 3-hourly radiosonde observations at Syowa Station. *Journal of the Atmospheric Sciences*, *65*(12), 3719–3735. https://doi.org/10.1175/2008JAS2539.1

Scherhag, R. (1952). Die explosionsartige Stratosphärenerwärmung des Spätwinters 1951/52. *Berichte des Deutschen Wetterdienstes in der US-Zone*, *6*(38), 51–63.

Senf, F., & Achatz, U. (2011). On the impact of middle-atmosphere thermal tides on the propagation and dissipation of gravity waves. *Journal of Geophysical Research*, *116*(D24), D24110. https://doi.org/10.1029/2011JD015794

Simmons, A. J., & Burridge, D. M. (1981). An energy and angular momentum conserving vertical finite-difference scheme and hybrid vertical coordinates. *Monthly Weather Review*, *109*(4), 758–766. https://doi.org/10.1175/1520-0493(1981)109<0758:aeaamc>2.0.co;2

Siskind, D. E., Coy, L., & Espy, P. (2005). Observations of stratospheric warmings and mesospheric coolings by the TIMED SABER instrument. *Geophysical Research Letters*, *32*(9), L09804. https://doi.org/10.1029/2005GL022399

Siskind, D. E., Eckermann, S. D., McCormack, J. P., Coy, L., Hoppel, K. W., & Baker, N. L. (2010). Case studies of the mesospheric response to recent minor, major, and extended stratospheric warmings. *Journal of Geophysical Research*, *115*, D00N03. https://doi.org/10.1029/2010JD014114

Smith, A. K. (2012). Global dynamics of the MLT. *Surveys in Geophysics*, *33*(6), 1177–1230. https://doi.org/10.1007/s10712-012-9196-9

Smith, A. K., Garcia, R. R., Marsh, D. R., & Richter, J. H. (2011). WACCM simulations of the mean circulation and trace species transport in the winter mesosphere. *Journal of Geophysical Research*, *116*(D20), D20115. https://doi.org/10.1029/2011JD016083

Stober, G., Janches, D., Matthias, V., Fritts, D., Marino, J., Moffat-Griffin, T., et al. (2021). Seasonal evolution of winds, atmospheric tides, and Reynolds stress components in the southern hemisphere mesosphere-lower thermosphere in 2019. *Annales Geophysicae*, *39*, 1–29. https://doi.org/10.5194/angeo-39-1-2021

Stober, G., Kuchar, A., Pokhotelov, D., Liu, H., Liu, H.-L., Schmidt, H., et al. (2021). Interhemispheric differences of mesosphere-lower thermosphere winds and tides investigated from three whole-atmosphere models and meteor radar observations. *Atmospheric Chemistry and Physics*, *21*(18), 13855–13902. https://doi.org/10.5194/acp-21-13855-2021

Tomikawa, Y., Sato, K., Watanabe, S., Kawatani, Y., Miyazaki, K., & Takahashi, M. (2021). Growth of planetary waves and the formation of an elevated stratopause after major sudden warming in a T213L256 GCM. *Journal of Geophysical Research: Atmospheres*, *117*(D16), D16101. https://doi.org/10.1029/2011JD017243

Trinh, Q. T., Ern, M., Doornbos, E., Preusse, P., & Riese, M. (2018). Satellite observations of middle atmosphere-thermosphere vertical coupling by gravity waves. *Annales Geophysicae*, *36*(2), 425–444. https://doi.org/10.5194/angeo-36-425-2018

Vadas, S. L. (2007). Horizontal and vertical propagation and dissipation of gravity waves in the thermosphere from lower atmospheric and thermospheric sources. *Journal of Geophysical Research*, *112*(A6), A06305. https://doi.org/10.1029/2006JA011845

Vadas, S. L., & Becker, E. (2018). Numerical modeling of the excitation, propagation, and dissipation of primary and secondary gravity waves during wintertime at McMurdo station in the Antarctic. *Journal of Geophysical Research: Atmospheres*, *123*(17), 9326–9369. https://doi.org/10.1029/2017JD027974

Vadas, S. L., & Becker, E. (2019). Numerical modeling of the generation of tertiary gravity waves in the mesosphere and thermosphere during strong mountain wave events over the Southern Andes. *Journal of Geophysical Research: Space Physics*, *124*(9), 7687–7718. https://doi.org/10.1029/2019JA026694

Vadas, S. L., Fritts, D. C., & Alexander, M. J. (2003). Mechanisms for the generation of secondary waves in wave breaking regions. *Journal of the Atmospheric Sciences*, *60*(1), 194–214. https://doi.org/10.1175/1520-0469(2003)060<0194:mftgos>2.0.co;2

Vadas, S. L., & Nicolls, M. J. (2009). Temporal evolution of neutral, thermospheric winds and plasma response using PFISR measurements of gravity waves. *Journal of Atmospheric and Solar-Terrestrial Physics*, *71*(6–7), 740–770. https://doi.org/10.1016/j.jastp.2009.01.011

Vadas, S. L., Xu, S., Yue, J., Bossert, K., Becker, E., & Baumgarten, G. (2019). Characteristics of the quiet-time hotspot gravity waves observed by GOCE over the Southern Andes on 5 July 2010. *Journal of Geophysical Research: Space Physics*, *124*(8), 7034–7061. https://doi.org/10.1029/2019JA026693

Vadas, S. L., Zhao, J., Chu, X., & Becker, E. (2018). The excitation of secondary gravity waves from local body forces: Theory and observation. *Journal of Geophysical Research: Atmospheres*, *123*(17), 9296–9325. https://doi.org/10.1029/2017JD027970

Xu, S., Vadas, S. L., & Yue, J. (2021). Thermospheric traveling atmospheric disturbances in austral winter from GOCE and CHAMP. *Journal of Geophysical Research: Space Physics*, *126*(9), e2021JA029335. https://doi.org/10.1029/2021JA029335

Yamazaki, Y., Kosch, M. J., & Emmert, J. T. (2015). Evidence for stratospheric sudden warming effects on the upper thermosphere derived from satellite orbital decay data during 1967–2013. *Geophysical Research Letters*, *42*(15), 6180–6188. https://doi.org/10.1002/2015GL065395

Yasui, R., Sato, K., & Miyoshi, Y. (2018). The momentum budget in the stratosphere, mesosphere, and lower thermosphere. Part II: The in situ generation of gravity waves. *Journal of the Atmospheric Sciences*, *75*(10), 3635–3651. https://doi.org/10.1175/JAS-D-17-0337.s1

Zhang, F. (2004). Generation of mesoscale gravity waves in upper-tropospheric jet-front systems. *Journal of the Atmospheric Sciences*, *61*(4), 440–457. https://doi.org/10.1175/1520-0469(2004)061<0440:gomgwi>2.0.co;2

Zhang, S.-R., Erickson, P. J., Coster, A. J., Rideout, W., Vierinen, J., Jonah, O. F., & Goncharenko, L. P. (2019). Subauroral and polar traveling ionospheric disturbances during the 7–9 September 2017 storms. *Space Weather*, *17*(12), 1748–1764. https://doi.org/10.1029/2019SW002325

Zhang, S.-R., Erickson, P. J., Goncharenko, L. P., Coster, A. J., Rideout, W., & Vierinen, J. (2017). Ionospheric bow waves and perturbations induced by the 21 August 2017 solar eclipse. *Geophysical Research Letters*, *44*(24), 12067–12073. https://doi.org/10.1002/2017GL076054

Zülicke, C., & Becker, E. (2013). The structure of the mesosphere during sudden stratospheric warmings in a global circulation model. *Journal of Geophysical Research: Atmospheres*, *118*(5), 1–17. https://doi.org/10.1002/jgrd.50219

Zülicke, C., Becker, E., Matthias, V., Peters, D. H. W., Schmidt, H., Liu, H.-L., et al. (2018). Coupling of stratospheric warmings with mesospheric coolings in observations and simulations. *Journal of Climate*, *31*(3), 1107–1133. https://doi.org/10.1175/JCLI-D-17-0047.1